Spectrophotometric Properties of 162173 Ryugu's Surface from the NIRS3 Opposition Observations

Deborah Domingue[1], Kohei Kitazato[2], Moe Matsuoka[3], Yashiro Yokota[3], Eri Tatsumi[4,5,6], Takahiro Iwata[3], Masanao Abe[3], Makiko Ohtake[3], Shuji Matsuura[7], Stefan Schröder[8], Faith Vilas[1], Antonella Barucci[9], Rosario Brunetto[10], Driss Takir[11], Lucille Le Corre[1], Nicholas Moskovitz[12]

[1]Planetary Science Institute, Tucson AZ, USA; [2]University of Aizu, Fukushima, Japan; [3]Institute of Space and Astronautical Sciences, Japan Aerospace Exploration Agency, Japan; [4]Instituto de Astrofisica de Canarias, Tenerife, Spain; [5]Dept. of Astrophysics, Univ. of La Laguna, Tenerife, Spain; [6]Dept. Earth and Planetary Science, Univ. of Tokyo, Tokyo, Japan; [7]Kwansei Gakuin University, Nishinomiya, Japan; [8]DLR, Berlin, Germany; [9]LESIA, Observatoire de Paris, Université PSL, CNRS, Univ. de Paris, Sorbonne Université, France,; [10]Institut d'Astrophysique Spatiale, Orsay, France; [11]Jacobs/NASA Johnson Space Center, Houston, TX, USA; [12]Lowell Observatory, Flagstaff, AZ, USA.

Abstract: Examination of the opposition geometry properties show that Ryugu's surface regolith is commensurate with laboratory studies of the photometric behavior of powdered carbonaceous chondrites. The regolith is consistent with a broad grain-size distribution that contains a fine-grained component.
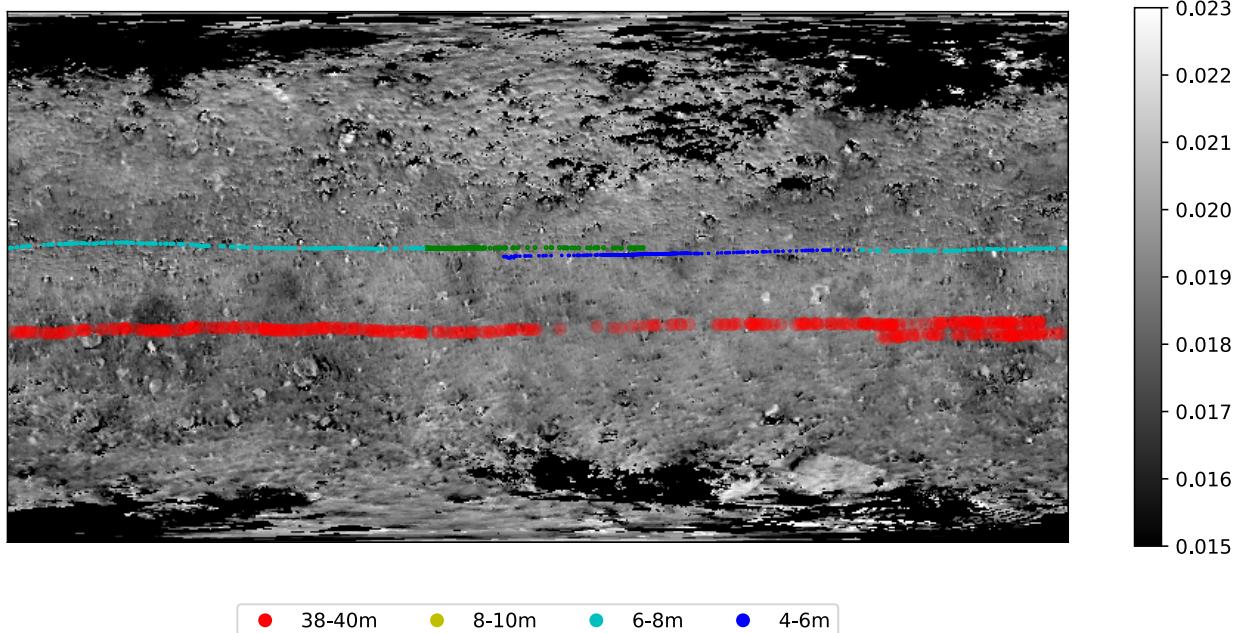
Fig. 1. NIRS3 footprints of the opposition observations used in this study overlaid on the ONC-T v-band standardized reflectance map (Tatsumi et al. 2020). The circles are sized to the footprint resolution of the spectra with blue representing 4-6 m resolution, cyan representing 6-8 m resolution, yellow representing 8-10 m resolution, and red representing 38-40 m resolution.

1.0 Introduction

Hayabusa2, the Japanese Aerospace Exploration Agency's (JAXA) spacecraft for the asteroid sample return mission to the near-Earth asteroid 162173 Ryugu, began conducting

remote sensing observation in June 2018. Among the observations were near-infrared (1.8 – 3.2 μm) reflectance measurements acquired by the Near Infrared Spectrometer (NIRS3). The NIRS3 is a point spectrometer with a 0.1° field-of-view which obtained continuous point-target spectra over Ryugu's surface. The observations used in this study are a subset of those made over the entire mission, and are those acquired by the NIRS3 prior to the first touchdown (TD1) for sample collection in February 2019. Included in this data set are infrared spectra of Ryugu acquired under opposition geometries (phase angles, α, <5°) at various spatial scales over the near-equatorial, low latitude regions (**Fig. 1**).

The surge in brightness near opposition is a characteristic of all particulate media. Its amplitude and width are a function of a variety of physical characteristics, including composition, grain size and shape, and porosity (e.g. Hapke 2012). This study examines the opposition data acquired by NIRS3 prior to the first sample collection. It examines the effects of footprint resolution, variability across the surface, and variations as a function of wavelength. The goal is to gain an understanding of the nature and magnitude of the surface variations on Ryugu. The opposition observations provide insight into the nature and properties of Ryugu's surface under unique observing conditions.

2.0 The Data Set

For this study, all observations acquired prior to TD1 were binned according to footprint resolution in consecutive bins of 2 m beginning with the first bin of 4 – 6 m footprint size. This resolution range (2m) was chosen as the smallest resolution with sufficient data to cover the incidence, emission, and phase angle space for modeling. All data for which geometric information (latitude, longitude, altitude, incidence, emission, and phase angle) was available were examined for this analysis. Each bin was examined for phase angle coverage. Only four footprint size bins contained opposition observations: bin 4-6m, bin 6-8m, bin 8-10m, and bin 38-40m. These four bins were used for this study of the opposition surge. All data within each footprint size bin, regardless of phase angle value, were used for the study.

Each spectrum ranges in wavelength from 1.8 – 3.2 μm (Iwata et al. 2017). This analysis focuses on the 76 channels ranging in wavelength from 1.801 – 3.149 μm. This wavelength range was selected since those channels above 3.2 μm are affected by thermal emission and those channels below 1.8 μm are within the wavelength region where the NIRS3 detector sensitivity decreases (Iwata et al. 2017, Kitazato et al. 2019). The observations were converted to reflectance using the calibration algorithm described in Iwata et al. (2017).

The data within each footprint size bin were organized into photometric angular groups. The groups were defined by every 1° of incidence and emission angle and every 0.1° of phase angle for observations acquired in the opposition region (α<5°). Groups outside the opposition region were defined by every 1° of incidence and emission angle and every 1° of phase angle. A representative spectrum for each angular group was selected at random. This method was selected to keep angle values connected to actual reflectance values. These representative spectra from each angular group, along with their photometric angle values, comprised the data set that was modeled. The modeling effort is described in Section 3.0. The results are examined both as a function of footprint size and as a combined, collective group.

A summary of the general spectral and photometric characteristics of the data set include:

- The smaller footprint resolution bins (< 10m) represent terrains north of the equatorial ridge while the largest footprint resolution bin (38-40m) represents terrains south of the equatorial ridge (**Fig. 1**).
- The footprints within each footprint resolution bin fall on different albedo terrains (**Fig. 1**).
- The angular groups display some variability (~10%) within the spectra contained in that group, independent of footprint resolution bin (**Fig. 2**).
- Spectral properties are uniform between different footprint bins (**Fig. 3**).
- The phase curve in the opposition region displays both wavelength and footprint resolution bin related variations (**Fig. 4**).
- The phase curve at larger phase angles (α >10°) shows no variations with footprint resolution bin, but wavelength dependent variations are observed at a few phase angles > 16°, which may be a consequence of the incidence and emission angle coverage (**Fig. 4**).

2.1 Spectral properties of the Data Set

The NIRS3 spectra in the 1.8 to 3.2 μm range show a fairly flat spectrum with a sharp absorption feature at ~2.7 μm, indicative of the presence of hydroxyl (OH) – bearing minerals (Kitazato et al. 2019). These spectral characteristics are ubiquitous over the surface (Kitazato et al. 2019), however we do see some variations in overall albedo and depth of the 2.7 μm feature across the surface (Barucci et al. 2019).

Many angular bins do not contain any data. Those angular bins that are present in the data set contain a small number of spectra (**Fig. 2** displays an example for the 6-8m footprint group of spectra acquired within angular bin $4° < i < 5°$, $8° < e < 9°$, $12° < \alpha < 13°$). Spectral variability is predominately in albedo, not in spectral slope or the absence/presence of spectral features (**Fig. 3**). This is attributed to local differences in Ryugu's surface, and is discussed in more detail in Section 2.3. The small variations observed in the spectra are the result of calibration residuals and not Gaussian photon noise.
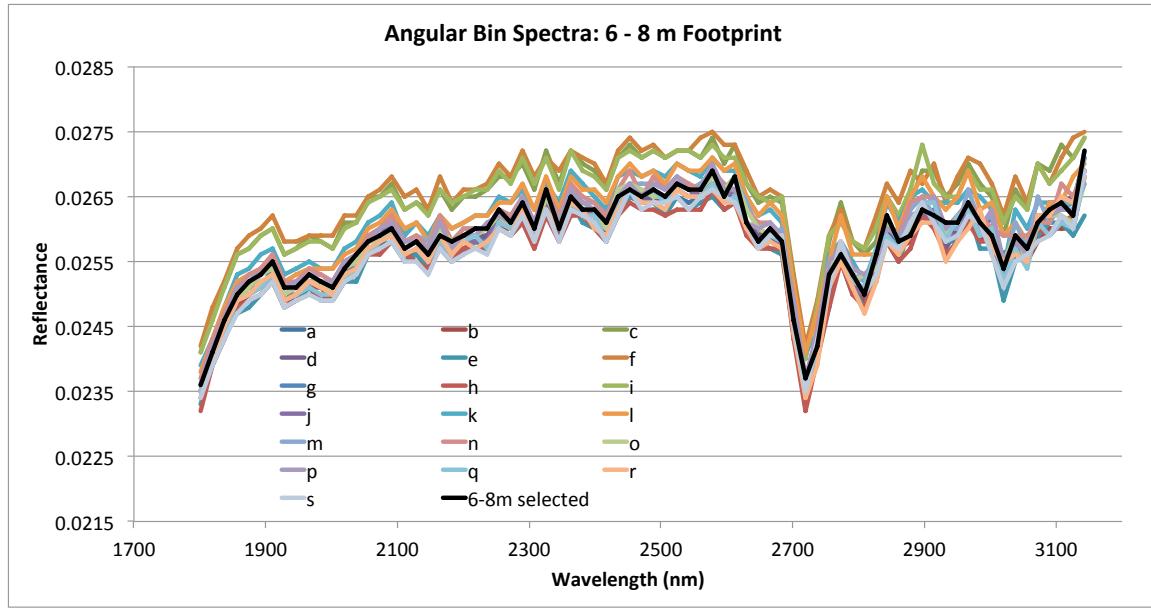
Fig. 2. The spectra shown are from the angular bin with incidence angle of 4° – 5°, emission angle of 8° – 9°, and phase angle of 12° – 13° from the 6 – 8 m footprint resolution group. All spectra from this angular bin and footprint resolution group (labeled alphabetically) are displayed. The representative spectrum for this angular bin and footprint resolution group is shown as a solid black line. The small variations are due to calibration residuals.

2.2 Photometric characteristics of the Data Set

Another method for examining the spectral data is to look at the variations in reflectance as a function of phase angle with respect to wavelength. Comparisons of the phase curve (reflectance vs phase angle) at various wavelengths shows that the NIRS3 phase curve varies with wavelength, most notably within the opposition region (**Fig. 4**). Examination of the phase curve at 2μm, 2.56μm, and 2.7μm (**Fig. 4**) shows that for each illumination and viewing geometry, the reflectance as a function of phase angle is wavelength dependent, and possibly dependent on footprint resolution.
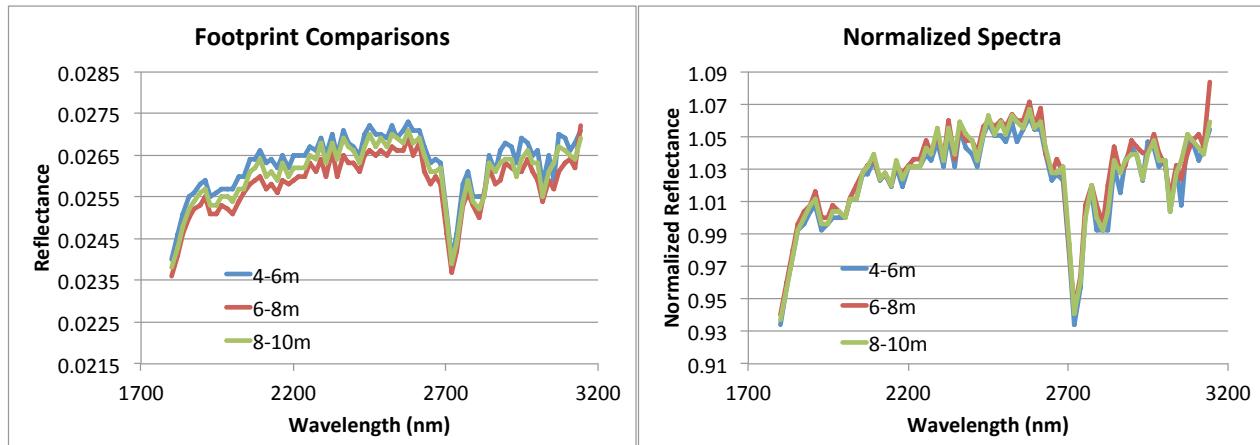

Fig. 3. The representative spectra from the angular bin with incidence angle of 4° – 5°, emission angle of 8° – 9°, and phase angle of 12° – 13° from the three footprint resolution

groups that contain spectra within this angular range. The spectra are shown absolute reflectance (left) and normalized to unity at ~2 µm (right).
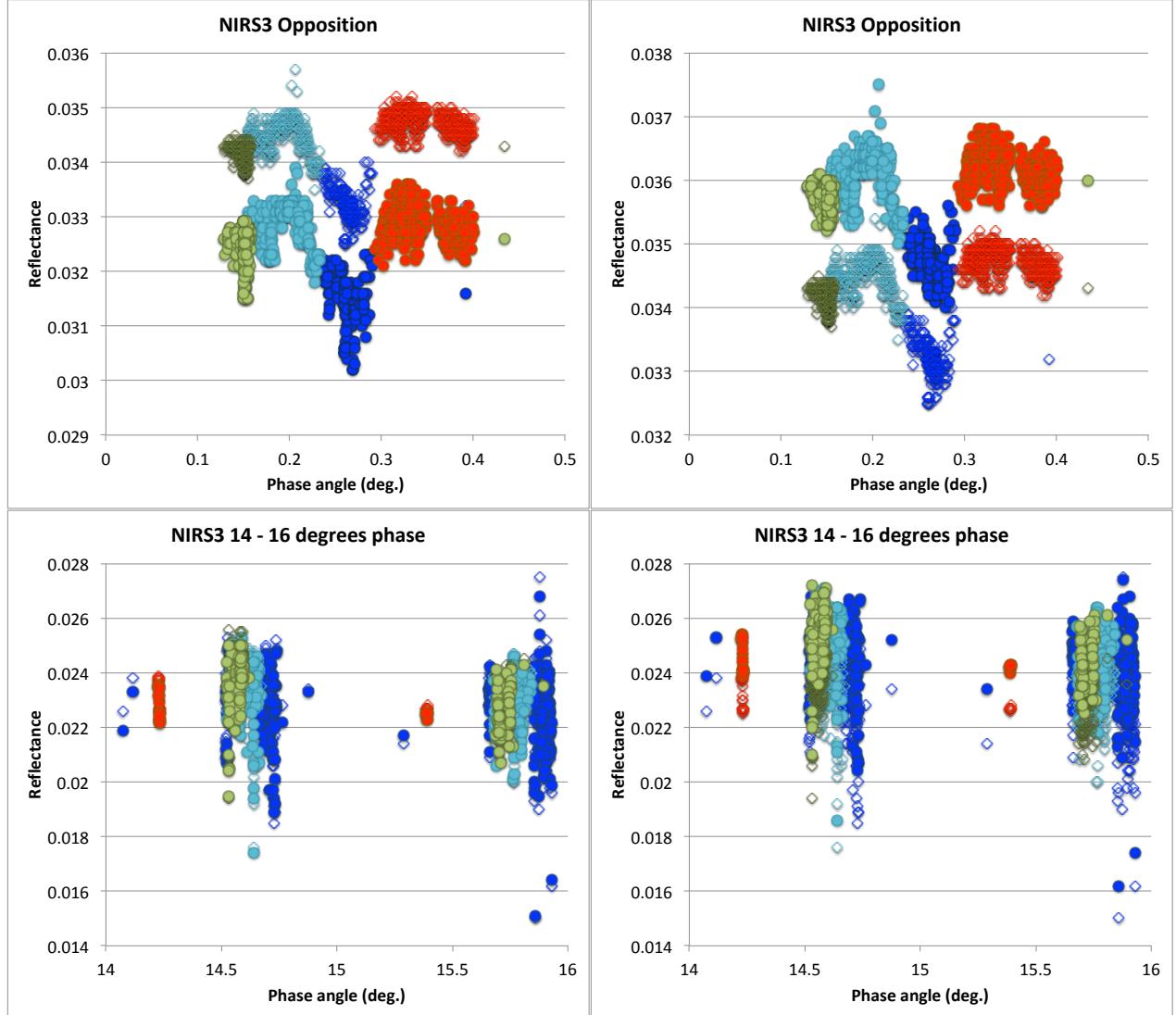

Fig. 4. Different regions within the NIRS3 phase curve are shown comparing three different wavelengths and all four footprint-resolution groups. The size groups are represented by the same colors as in Fig. 1. The left column compares the phase curve at 2µm (open diamonds) and 2.7µm (solid circles). The right column compares the phase curve at 2µm (open diamonds) and 2.56µm (solid circles). The top row displays the opposition region and the bottom row displays the 14° – 15° phase range. There are wavelength dependent differences seen in at the opposition phase angles that are not present at the higher phase angles.

3.0 Model and Modeling Methodology

The data sets from each footprint resolution bin were combined to form a data set for modeling the opposition region of Ryugu's phase curve. The data range in phase angle from

0.128° to 28.141°. The incidence and emission angle coverage is shown in **Fig. 5**. Here we describe the model used and the approach taken with the model application.
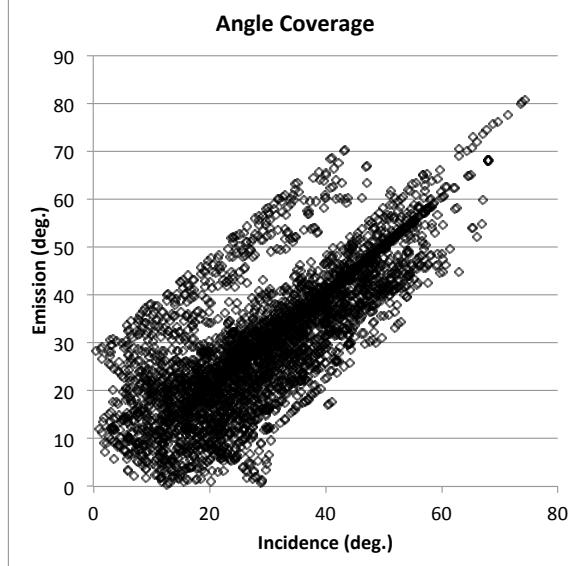

Figure 5. This graph displays the coverage in incidence (i) and emission angle (e) of the opposition data set examined in this study.

3.1 The Model

The model used to analyze the NIRS3 data set is that described by the Hapke set of equations for expressing disk-resolved reflectance, *(I/F)$_R$*, which is given by:

$$\left({}^I/_F\right)_R = \frac{w}{4}\frac{\mu_{0e}}{\mu_{0e}+\mu_e}\left\{[P(\alpha)[1+B(\alpha)]] + [H(\mu_{0e})H(\mu_e)-1]\right\}S(i,e,\alpha,\bar{\theta}) \quad Eq(1),$$

where *w* is the single scattering albedo, *P(a)* is the single particle scattering function (Eq. 2), and *B* is the opposition term (Eq. 3). For this study a single-term Henyey-Greenstein function was chosen for *P(a)*, such that

$$P(\alpha) = \frac{(1-b^2)}{[1-2b\cos(\alpha)+b^2]^{3/2}} , \quad Eq(2)$$

where *b* describes the amplitude of the scattering peaks. Postitive values of *b* correspond to backward scattering, negative values to forward scattering. A single term phase function is used since the data set does not capture the forward scattering direction (a >110°) and only contains observations with phase angle values below 30°.

The opposition term, *B(α),* in this expression is given by

$$B(\alpha) = \frac{B_{S0}}{1 + \frac{\tan\left(\alpha/2\right)}{h_s}} , \quad Eq(3)$$

6

where B_{S0} describes the amplitude of the opposition surge and h_s describes the width of the opposition peak. This expression assumes that the shadow-hiding mechanism (SHOE) is the sole contributor to the opposition effect. This assumption is made since Ryugu's albedo is extremely low; it is one of the darkest objects to be visited by a spacecraft.

In the disk-resolved reflectance equation (Eq. 1) the surface roughness term, $S(I,e,\alpha,\bar{\theta})$, accounts for the large-scale roughness, and μ_{0e} and μ_e are the modified cosines of the incident and emission angles, respectively, due to surface roughness. The surface roughness is defined as the average surface tilt on the size scale ranging from a few particle diameters to the resolution of the detector footprint (e.g Hapke 2012). The $H(x)$ terms in the reflectance equation are the Chandrasehkar H-functions. The mathematical expressions for these terms, and their derivation can be found in Hapke (1981, 1984, 1986, 1993, 2002, 2008, 2012).

3.2 Modeling Methodology

The modeling methodology used was a least squares grid search that minimized the value of chi (χ), defined by

$$\chi = \frac{\sum_{i=1}^{N} \sqrt{(r_{measured} - r_{model})^2}}{N}, \text{Eq(4)}$$

where N is the number of measurements, $r_{measured}$ is the NIRS3 measured reflectance, and r_{model} is the calculated reflectance using the Hapke model. The grid search was defined by a range and increment (grid size) for each parameter, and all combinations across the parameter values were examined. All parameters were varied simultaneously, and the top ten parameter sets that resulted in the lowest values of chi were recorded. This is the same methodology used by Domingue et al. (2016a, 2016b, 2018). Each wavelength channel was modeled independently.

The initial grid size for w was 0.005, B_o was 0.05, h and b was 0.01, and $\bar{\theta}$ was 5°. The final grid size was 0.001 for w, 0.005 for B_o, 0.001 for h and b, and 1° for $\bar{\theta}$. The range in values for each parameter depended on the model run since the data was modeled in a step-wise fashion. In the initial modeling run, where a run is where all the wavelengths have been modeled using the same parameter constraints, the only constraint was placed on the opposition amplitude parameter, B_o. In this initial run B_o was constrained to be less than unity. This is in line with Ryugu's surface being dark and the dominant mechanism for producing the opposition surge is shadow-hiding. The parameter ranges for the initial run were 0.03 – 0.06 for w, 0 – 1 for B_o, 0.001 – 0.171 for h, 0.20 – 0.55 for b, and 10 – 35 for $\bar{\theta}$. These ranges were based on the model values obtained by Tatsumi et al. (2020) for the Telescopic Optical Navigation Camera (ONC-T) modeling efforts.

Prior to the second step, the values of the surface roughness parameter and the single particle scattering function parameter were examined. The median value of the surface roughness parameter, $\bar{\theta}$, across all wavelengths, was found to be 29° with a range of values between 28° – 31° over all wavelengths. Thus, for the second run, the value of $\bar{\theta}$ was constrained to be 29°. In the derivation of the Hapke model equations, the value of $\bar{\theta}$ is defined to be wavelength independent, thus constraining the value of $\bar{\theta}$ to 29° across all wavelengths is in line with the definition of this parameter.

The phase angle coverage in this data set only samples the backward scattering direction, thus this study utilized only a single-term Henyey-Greenstein single particle scattering function (Eq. 2) for $P(\alpha)$. However there is a mathematical coupling in the Hapke equations between w, $P(\alpha)$, and $\bar{\theta}$, especially over this small phase angle range (i.e. Hapke 2012). Using the median value of $\bar{\theta}$ across all wavelengths not only aligns with the parameter's derivation and definition, but also assists in decoupling the values of these three parameters. In addition, the value of $P(\alpha)$ also affects the opposition terms over this phase angle range dominated by the opposition region. The values of w, B_o, h, and b after the initial run all displayed strong wavelength variations, especially between 2.4 to 3.0 μm. In order to eliminate mathematical coupling as the source of these wavelength dependencies, the value of the single particle scattering function parameter, b, was set to the median value over wavelengths from 1.8 – 2.4 μm. The median value of b, in this wavelength range, is 0.318 over a range of values from 0.315 – 0.324.

In the second, and final run, the parameters w, B_o, and h were varied while the value of b was set to 0.318 and the value of $\bar{\theta}$ was set to 29°. The initial/final grid size was 0.001, 0.005, and 0.001 for w, B_o, and h, respectively. The parameter value ranges were 0.04 – 0.06, 0.3 – 1, and 0.01 – 0.21 for w, B_o, and h, respectively. The parameter values, as a function of wavelength, after the initial run and after the final run are compared in **Fig. 6**.
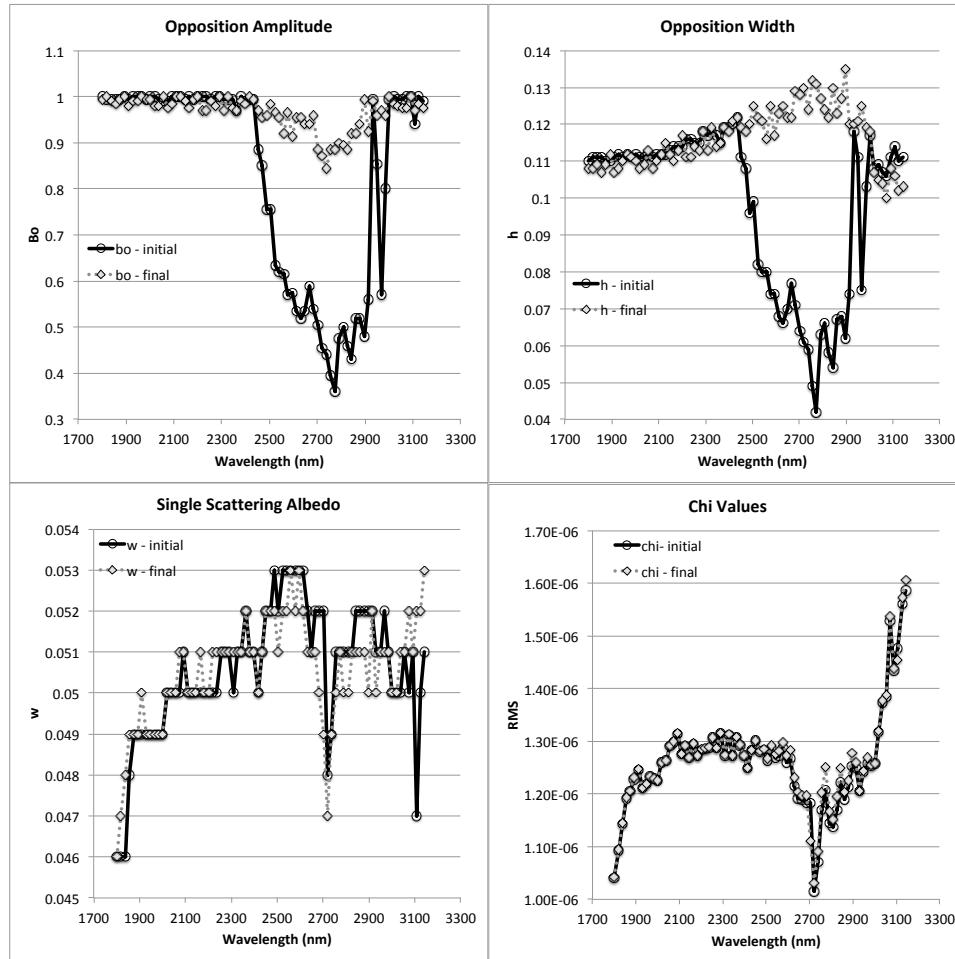
Figure 6. These graphs compare and contrast the model parameter and χ values from the initial modeling run with the final modeling run as a function of wavelength. The initial run values are shown by the solid black lines (circles) and the final run values are shown by the dotted grey lines (diamonds).

4.0 Modeling Results
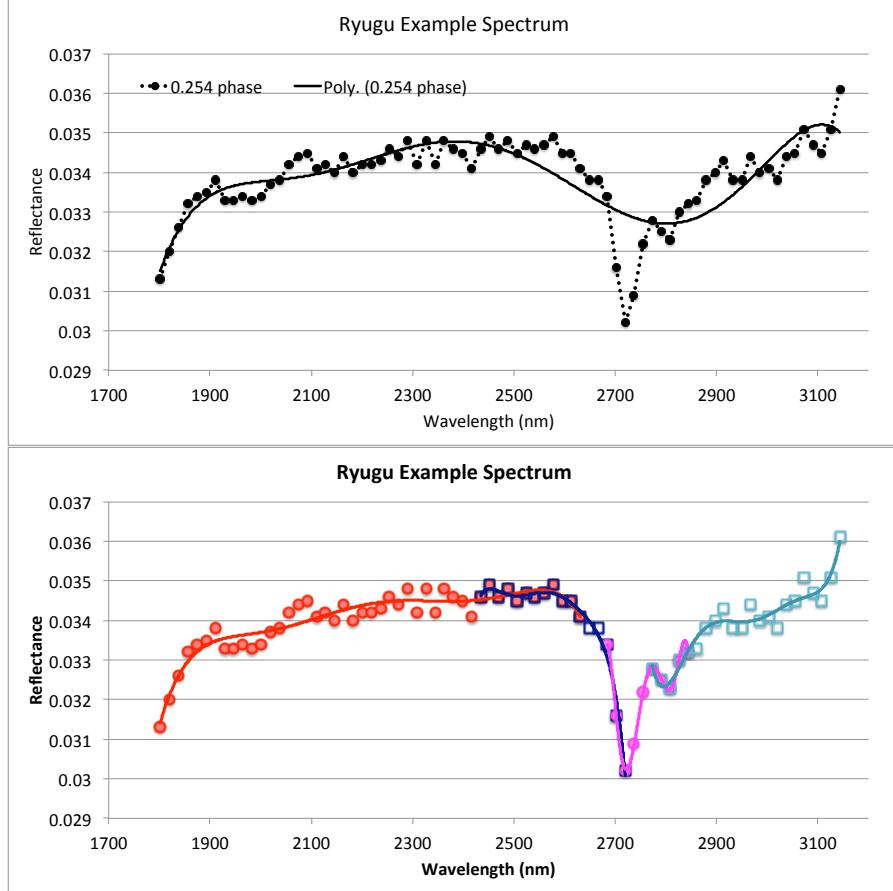
Figure 7. Variability of the NIRS3 spectra with wavelength. The top graph displays an opposition spectrum acquired at 0.254° phase modeled with a 6th order polynomial. The central graph displays the same spectrum divided into 4 wavelength segments (color-coded red, navy, pink, and teal), each modeled with a separate 6th order polynomial.

Examination of the parameter values in **Fig. 6** show that they are not a smooth function of wavelength (they include variations due to compensations for the calibration residuals). For example, the single scattering albedo final values show a constant value of 0.049 between 1.86 μm – 2.0 μm, except for at 1.91 μm where the value is 0.050. These values are equivalent within the error estimates (w: ±0.002). This level of variation is due to uncertainties in the spectral measurements, differences within the data set from variations in Ryugu's surface reflectance, and the search grid increment that all translate into uncertainties in the parameter values. In order to ensure that any standardizations using the model values to do not introduce spurious spectral variations, it is important to derive parameter values that are smooth, yet variable, as a function of wavelength, such that the wavelength-to-wavelength deviations should not contain spurious spikes or dips.

9

One technique for deriving parameter values that minimizes wavelength-to-wavelength variations is to apply a polynomial fit to the parameter values (Domingue et al. 2015, 2016a). However, as shown in **Figure 7**, the spectrum of Ryugu itself is not well fit by a single polynomial of order 6 or less. Important spectral features are lost or highly diminished if a single polynomial is used to fit the entire wavelength range of the spectrum. In order to capture the spectral variations in the spectrum, the spectrum was divided into four wavelength segments, and each segment was fit with a 6th order polynomial. The segments were defined such that they overlapped with adjacent segments (contained data points in common), and that the polynomial fits could provide a smooth transition between segments. When spliced together the concatenated polynomials provided a smooth curve descriptive of the spectrum, as demonstrated in **Figure 7**.

In order to avoid loss of spectral variability in the photometric parameters a similar approach was taken to fitting the parameter values with a series of polynomials as demonstrated on the NIRS3 spectrum. Using the wavelength segments defined by the example spectrum (**Fig. 7**), the parameter values were divided into similar segments and fitted with 6th order polynomials. The resulting parameter values from the polynomial fitting are shown in **Fig. 8** as a function of wavelength.

The ratio between the observed reflectance to the model predicted reflectance (**Fig. 9**) was calculated in order to examine how well the model describes the data set. Values of unity correspond to equivalent values between the observation and model. Over the entire phase curve examined 74.5%, 82.5%, 78.8%, and 86.0% of the 4 – 6m, 6 – 8m, 8 – 10m, and 38 – 40m footprint groups, respectively, have ratio values within 5% of unity. If we examine the percentage of ratio values within 2% of unity we find that over the entire phase curve examined 39.9%, 53.7%, 48.2%, and 63.5% of the 4 – 6m, 6 – 8m, 8 – 10m, and 38 – 40m footprint groups, respectively, fall in this range. Within the opposition region ($\alpha < 1°$) 82.8%, 99.6%, 100%, and 100% of the 4 – 6m, 6 – 8m, 8 – 10m, and 38 – 40m footprint groups, respectively, have ratio values within 5% of unity. The percentage of modeled observations that fall within 2% of unity within the opposition region are 81.0%, 52.2%, and 100% of the 6 – 8m, 8 – 10m, and 38 – 40m footprint groups, respectively, while none of the 4 -6m footprint group model values are within 2% of the observations.

Another test of the modeling results is an examination and comparison of how well the model replicates the spectral properties of the spectral data set. Examples of spectral observations acquired near 15° phase (**Fig. 10**) and within the opposition region (**Fig. 11**) are contrasted with corresponding spectra derived from the Hapke model solutions. In the examples shown from the near 15° phase observations, there are good replications of the spectra by the model at 15.756° phase, yet poor replications at 15.766° phase. Normalizing the 15.766° phase spectra to unity at 2.5 μm (**Fig. 10**) shows that both the observed spectra and their corresponding model spectra overlap. This is also observed at other phase angles. This suggests that the variations we are seeing are due to albedo variations across the surface and not wavelength-to-wavelength (spectral) differences. **Figure 10** demonstrates that within the data set there is a range of reflectance values for similar viewing conditions, which the modeling attempts to minimize. However, this figure also demonstrates that the modeling results do not introduce any spurious spectral variations. A similar examination of the spectra acquired at near opposition geometries (**Fig. 11**) shows that the model better predicts the spectral properties near opposition than at larger phase angles.

Single Scattering Albedo

Opposition Amplitude

Opposition Width
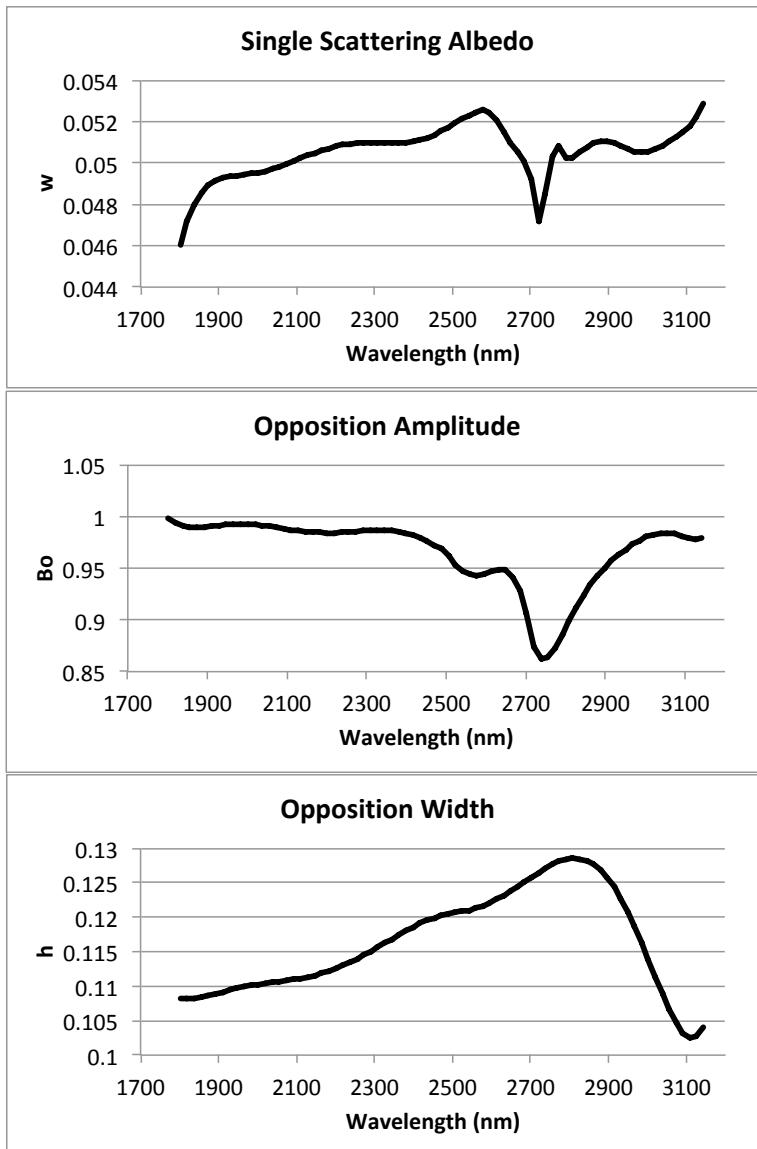
Figure 8. Hapke model parameter values as a function of wavelength after the polynomial fitting of the final model results. The feature in the single scattering albedo at 2.7 µm is a reflection of the absorption seen in the spectral data at this wavelength, while other broad features are a result of variations in the data set due to more subtle slope variations within the data sets.
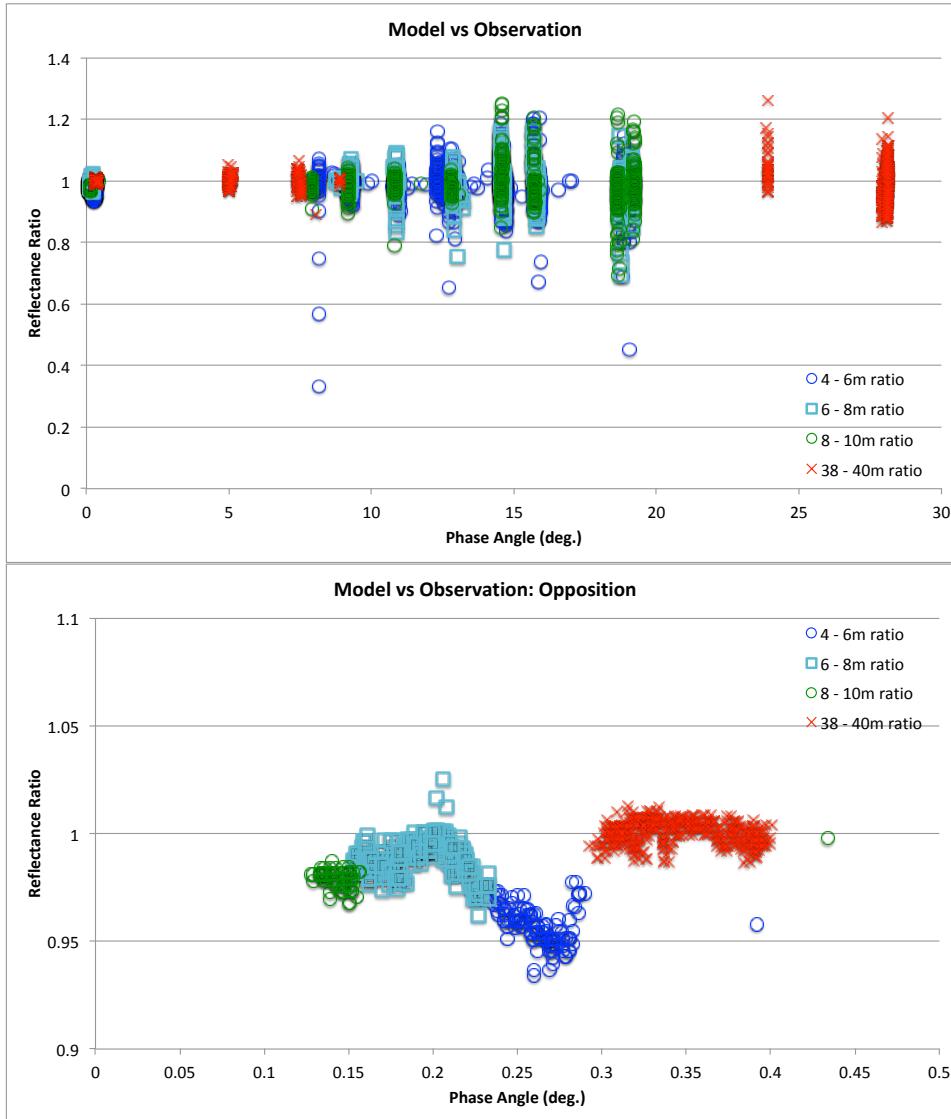
Figure 9. As a test of the goodness of fit the ratio of the observed reflectance to the model predicted reflectance is plotted as a function of phase angle for the 2.0 μm data set over all the footprint resolution groups. These results are typical of those seen across all wavelengths.
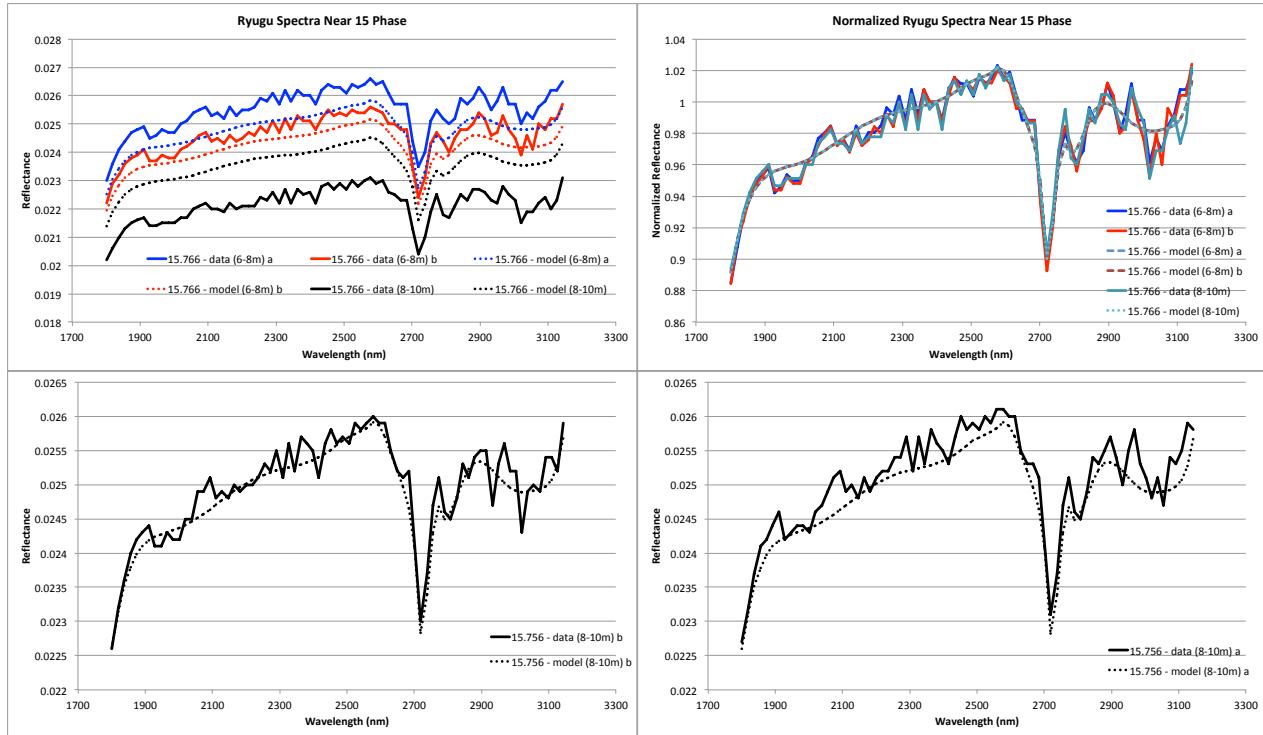
Figure. 10. Comparisons of spectral observations from NIRS3 (solid lines) near 15° phase with the corresponding model predicted spectra (dashed lines). Comparisons are made in absolute reflectance (top left, bottom row) and normalized to unity at 2.5 μm (top right).
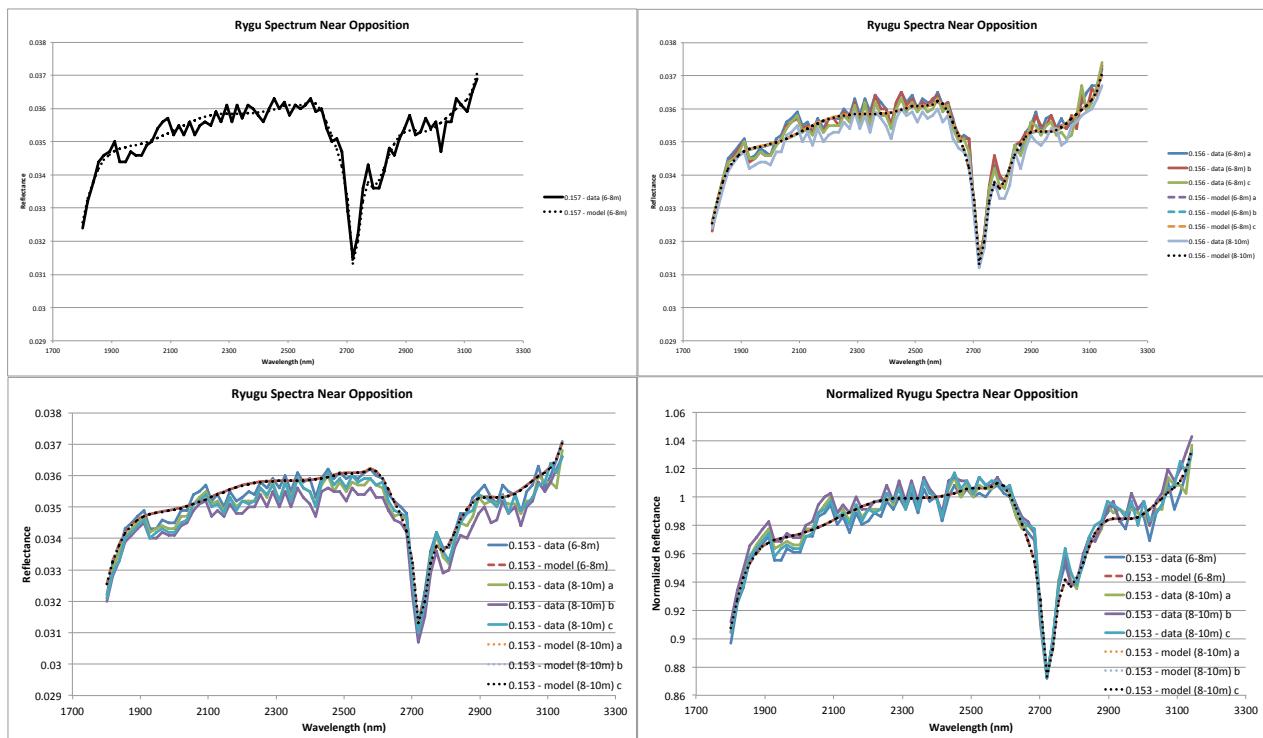
Figure 11. Comparisons of spectral observations from NIRS3 (solid lines) near opposition with the corresponding model predicted spectra (dashed lines). Comparisons are made in absolute reflectance (bottom left, top row) and normalized to unity at 2.5 µm (bottom right).
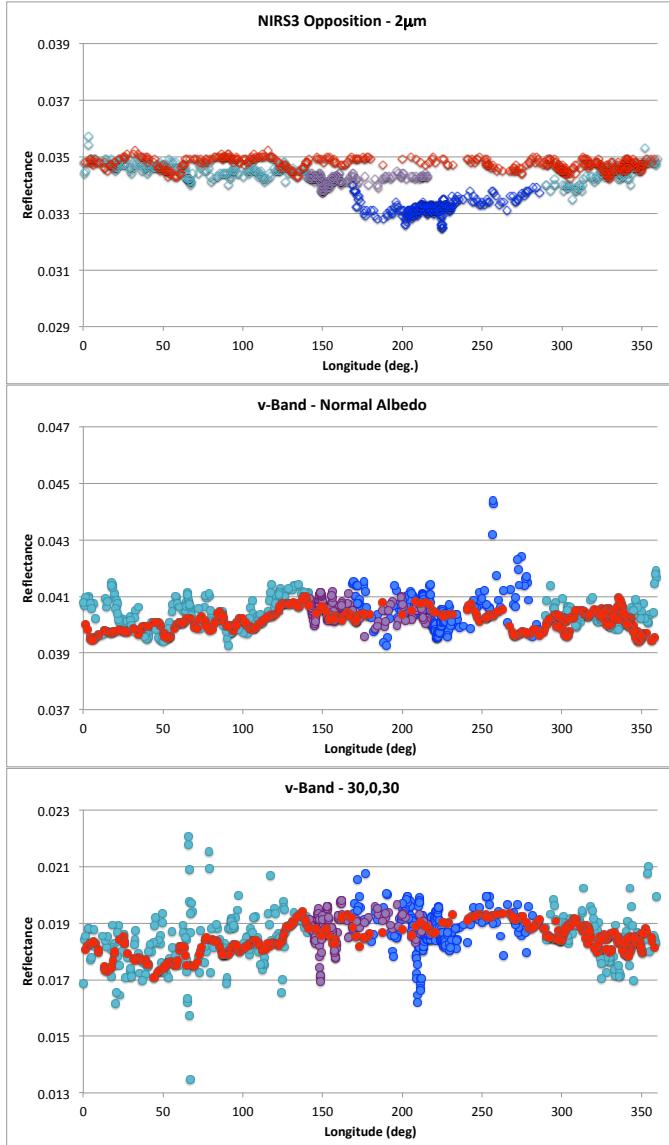
Fig. 12. The reflectance variation within the NIRS3 opposition data (top) acquired at phase angles <5° is compared with the NIRS3-equivalent footprint resolution data extracted from the ONC-T v-band standardized mosaic (center, Tatsumi et al. 2020) and the ONC-T v-band normal albedo mosaic (bottom, Yokota et al. 2020). Size group colors as in Fig. 1. Phase angles below 1° range from 0.293° – 0.401° for the 4-6m resolution bin, 0.150° – 0.233° for the 6-8m resolution bin, 0.128° – 0.434° for the 8-10m resolution bin, and 0.293° – 0.401° for the 38-40m resolution bin.

5.0 Comparisons with ONC-T
5.1 Comparisons of Spectral Properties

Comparisons of the NIRS3 opposition observations were made with the ONC-T color observations. Two sets of mosaics have been created from the ONC-T data set. One set of mosaics were constructed from images photometrically standardized to 30°, 0°, 30° in incidence, emission, and phase, respectively (Tatsumi et al. 2020). This set consists of a global mosaic for each filter band of the camera system, and we here after refer to these global mosaics as the 'standard mosaics'. The second set of mosaics was constructed from the ONC-T opposition observations and they represent the normal albedo of the surface (Yokota et al. 2020). This set also consists of global mosaics, one for each band, and we here after refer to these global mosaics as the 'normal albedo mosaics'. The locations of the NIRS3 opposition observations are shown on the v-band standard mosaic in **Fig. 1**.

Initial comparisons between the NIRS3 opposition spectra and the ONC-T observations were made by comparing the NIRS3 2.0 µm band reflectance as a function of longitude with the ONC-T equivalent reflectance extracted from both the v-band standard mosaic and the v-band normal albedo mosaic as a function of longitude (**Fig. 12**). The ONC-T equivalent spectra are derived from the global mosaics by projecting the NIRS3 footprint onto the mosaic and calculating the median value of the pixels contained within the footprint. The v-band equivalent reflectance values from both v-band mosaics show no reflectance differences as a function of footprint resolution. The NIRS3 reflectance values indicate that the smallest footprint resolution bin (4-6m) is different than the remaining footprint resolution bins. However, the spread in reflectance values between the 4-6m footprint resolution bin and the other NIRS3 footprint resolution bins is comparable to the spread seen in the v-band equivalent data (**Fig. 12**). The range in reflectance values in the v-band equivalents is larger than the range seen in the NIRS3 2.0 µm data.

Spectral properties that can be examined, and compared to laboratory studies of meteorites, include spectral slope and phase reddening. Spectral slope is defined as

$$slope = \frac{R_1 - R_2}{\lambda_1 - \lambda_2},$$

where R_1 and R_2 are the normalized reflectance values at wavelengths λ_1 and λ_2, respectively. A spectrum is considered 'red' or 'red sloped' if it becomes brighter as wavelength increases, or the slope is positive. Conversely, a spectrum is considered 'blue' or 'blue sloped' if it becomes darker with increasing wavelength, or the slope is negative. Phase reddening (P_r, also called spectral reddening in the literature) is defined as

$$P_r = \frac{slope_{\alpha 1} - slope_{\alpha 2}}{\alpha 1 - \alpha 2},$$

where $\alpha 1$ and $\alpha 2$ are phase angle values and their corresponding slopes. Phase reddening occurs when P_r is larger than zero (slope increases with increasing phase angle), and phase bluing occurs when P_r is less than zero (slope decreases with increasing phase angle).

The spectral slope at the NIRS3 opposition footprint sites can be examined in both the visible and the near-infrared. Using the ONC-T data, the visible spectral slope was calculated using the b- and p-bands reflectance values normalized to the v-band. The slope was calculated for the locations of the NIRS3 opposition data from both the normal albedo

mosaics of Yokota et al. (2020), and the standard mosaics of Tatsumi et al. (2020) (**Fig. 13**). The standard mosaics represent the reflectance at 30° phase while the normal albedo mosaics represent the reflectance at 0° phase. The slope values derived from the normal albedo mosaics is blue while the corresponding values from the standard mosaic are red, thus indicating that the visible spectral properties become more red with increasing phase angle (**Fig. 13**), commensurate with the studies of Sugita et al. (2019) and Tatsumi et al. (2020).

The spectral slope within the NIRS3 data was calculated based on the wavelength interval between 1.9 μm to 2.5 μm normalized to unity at 2.0 μm, using the NIRS3 data from opposition (α<0.5°) and again using data from 18.5° – 19.5° phase (**Fig. 14**). The near opposition and near 19° phase slopes are both red, and in the near-infrared Ryugu's surface exhibits subtle phase reddening (becomes 'more red', the slope increases with increasing phase angle). The phase reddening values are 4.5×10^{-6}, 4.2×10^{-6}, 4.4×10^{-6}, and 5.1×10^{-6} (units of $\mu m^{-1} deg^{-1}$) for the 4 – 6m, 6 – 8m, 8 – 10m, and 38 – 40m footprint bins, respectively. These values are calculated from the median spectral slope for each footprint bin for both the near opposition and near 19° phase spectra. This is in comparison to the visible phase reddening values of 3.9×10^{-3}, 4.4×10^{-3}, 3.4×10^{-3}, and 2.4×10^{-3} (units of $\mu m^{-1} deg^{-1}$) for the 4 – 6m, 6 – 8m, 8 – 10m, and 38 – 40m footprint bins, respectively, calculated from the normal albedo and standard mosaics (**Fig. 13**). The visible phase reddening values are higher than those calculated by Tatsumi et al. (2020) of $(8 \pm 5) \times 10^{-4}$ $\mu m^{-1} deg^{-1}$, which is based on a disk-integrated data set. Thus phase reddening is observed in both visible and near-infrared spectra of Ryugu, although it is subtle and much shallower in the near-infrared wavelength range.
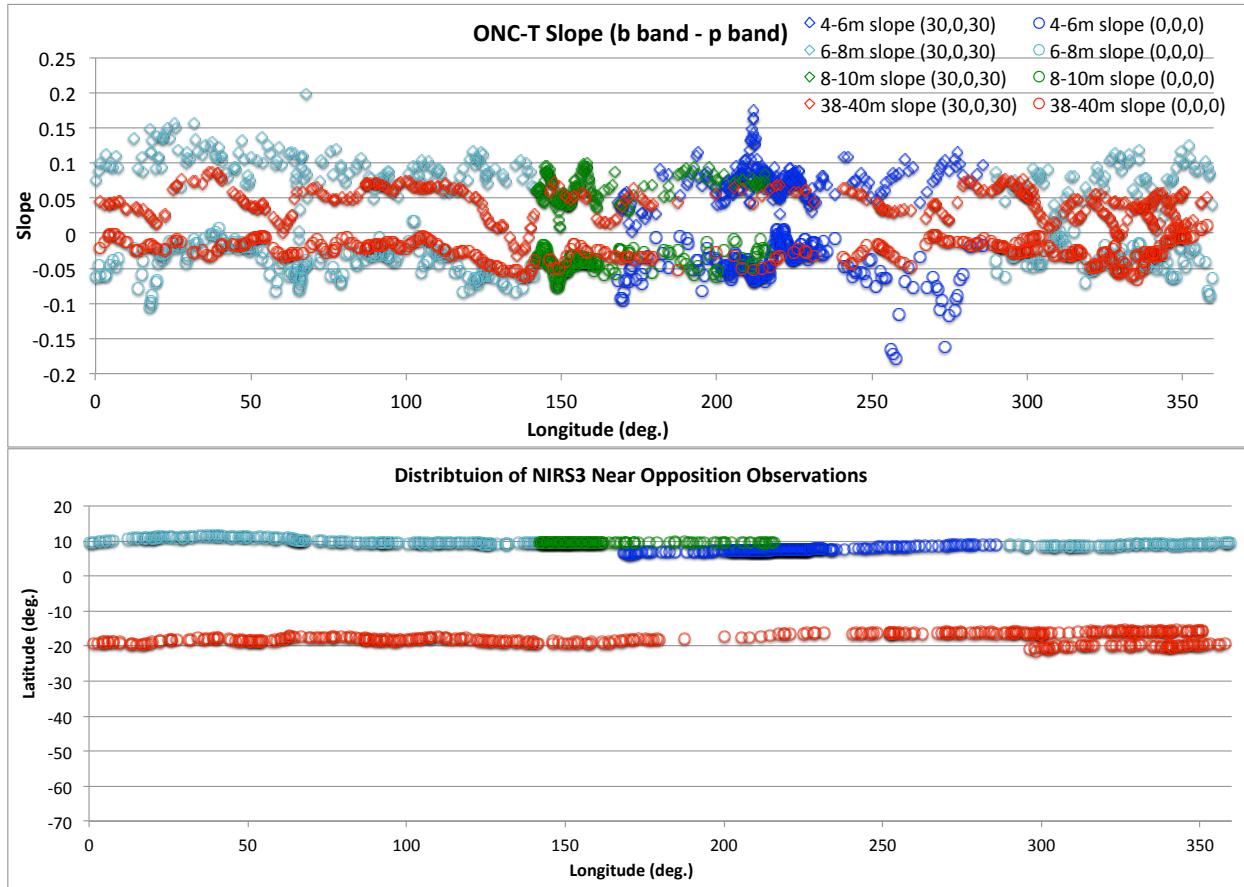
Figure 13. (top) The spectral slope calculated from the ONC-T standardized mosaics (open diamonds) of Tatsumi et al. (2020) and the normal albedo mosaics (open circles) of Yokota et al. (2020) of the ONC-T equivalent reflectance to the NIRS3 opposition data in units of µm⁻¹. The slopes were calculated using the b- and p-band reflectance values. The colors correspond to the footprint sizes (blue 4 – 6m, teal 6 – 8m, green 8 – 10m, and red 38 – 40m). Subtle regional variations are noted in the spectral slope values. (bottom) The longitudinal and latitudinal coverage of the opposition observations.
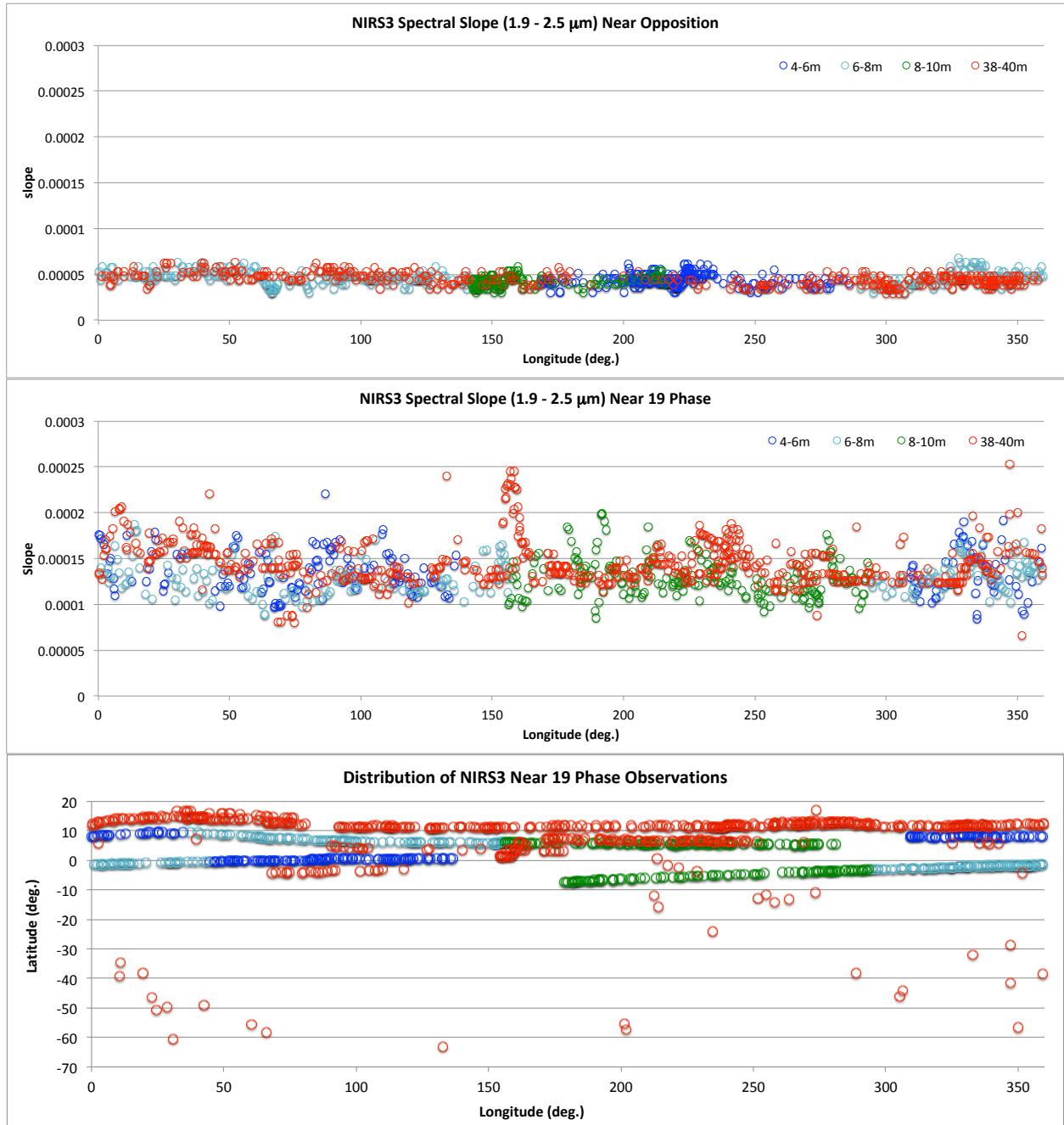
Figure 14. The spectral slope calculated from NIRS3 opposition observations (top) and the near 19 phase angle observations (center). The slopes were calculated using based on the 1.9 μm and 2.5 μm reflectance values. The colors correspond to the footprint sizes (blue 4 – 6m, teal 6 – 8m, green 8 – 10m, and red 38 – 40m). The longitudinal and latitudinal coverage of the near 19 phase observations (bottom) can be compared with the similar coverage for the opposition observations shown in Figure 13.

There have been many laboratory examinations of meteorite samples that have attempted to correlate spectral slope and phase reddening properties with asteroid regolith characteristics (e.g. Beck et al. 2012; Binzel et al. 2015; Cloutis et al. 2018). For example,

18

Beck et al. (2012) examined a series of meteorite samples over 5 different band pass filters in the visible (0.45 – 0.9 µm) that included three carbonaceous chondrites (Orgeuil (CI), Tagish Lake (CC), Allende (CV)) along with a howardite, eucrite, diogenite, and a lunar meteorite. All samples they examined displayed phase reddening. This trend with phase angle was seen in samples with both blue and red spectral slopes. This trend, also seen in studies of basalt and Allende meteorite (Gradie et al. 1980; Gradie and Veverka 1986), led Beck et al. (2012) to assert that phase reddening is ubiquitous to all meteorite types. More detailed laboratory work examined the correlations of spectral slope and spectral reddening with sample properties, such as granularity (rock vs powder), grain size, packing (porosity), and surface texture (roughness). The goal is to extrapolate these correlations to characterize the physical properties of asteroid surface regoliths. The findings are summarized and compared to our findings for Ryugu.

Granularity. Cloutis et al. (2018) examined and compared the spectral slope of samples of Murchison meteorite, a CM2 carbonaceous chondrite; finding that slab samples were darker and blue sloped in comparison with powdered samples. Examination of the Mukundpura CM2 chondrite by Potin et al. (2019) also correlated spectral effects as a function of rock versus powder. Potin et al. (2019) demonstrated that for samples of this CM2 meteorite, even though both powders and rock have red slopes, powder displays a redder spectral slope than the bare rock, and powder also displays greater phase reddening than rock. In their experiments they discovered that spectral slope is affected by incidence angle, where the powder sample was relatively insensitive to incidence but the rock sample displayed a strong sensitivity, especially at grazing (high) values of incidence. The effect they noted is that at the same phase angle, the spectral slope becomes redder with increasing incidence angle in their rock sample. This could be used as a test for the presence of powdered regolith on an otherwise rocky surface.

Examination of the NIRS3 38 – 40m footprint data as a function of incidence angle at both opposition and near 19° phase (**Fig. 15**) shows no definitive correlation in the spectral slope with incidence angle. This argues for a 'powder' component to Ryugu's regolith, based on the laboratory measurements described by Potin et al. (2019).

Grain Size. Binzel et al. (2015) examined Murchison samples of various grain sizes and demonstrated that while coarse-grained samples (500 – 1000 µm grains) are spectrally blue, the introduction of even 5% of a fine-grained fraction (< 45 µm grain size) changes the slope from blue to red. Increasing average grain size, for carbonaceous chondrites, results in darker more blue-sloped spectra (Johnson and Fanale 1973; Cloutis et al. 2011b, 2013, 2018; Gillis-Davis et al. 2013; Binzel et al. 2015), where as the inclusion or presence of a fine-grained fraction introduces spectral reddening (Schroder et al. 2014; Binzel et al. 2015; Cloutis et al. 2018). The spectral slopes here refer to the brightness variation at wavelengths above 0.7 µm. Cloutis et al (2018), in their study of Murchison powders, demonstrated that the greatest influence on spectral slope was the minimum grain size of the sample, not the average or maximum grain size. They showed that as the grain size decreases spectra become brighter and more red sloped, commensurate with the findings of Binzel et al. (2015).

Our analyses of the visible spectral slope properties shows that at opposition Ryugu's surface is blue sloped, where at larger phase angles (commensurate with those of the laboratory studies) the surface is red sloped. In the infrared the spectral slope is red at both

opposition and larger phase angles. Cloutis et al. (2018) demonstrated that slabs of a CM chondrite are blue, which would be expected of a surface with no granular regolith. Binzel et al. (2015) demonstrated that coarse-grained regolith also displays a blue spectral slope and that a fine-grained component was needed to produce a red spectral slope. Both the ONC-T and NIRS3 spectral observations show a red spectral slope for Ryugu's surface, providing another indication for the presence of a 'powder' component within Ryugu's regolith and that this component contains a fine-grained fraction.

Packing/Porosity. The study by Cloutis et al. (2018) found that the spectral effects of sample packing or porosity was connected to the incidence, emission, and phase angle conditions under which the spectra were acquired. At the standard laboratory conditions (i=30°, e=0°, α=30°) they found there were no effects on spectral slope with packing, however they found that spectral slope increased (became more red) with increasing porosity for spectra acquired at i=e=45°. This is commensurate with the findings of Lantz et al. (2017) who demonstrated that unpacked powder of carbonaceous meteorite samples were darker and redder than the same sample compacted into pellets. There is currently no metric to correlate spectral slope with a specific packing or porosity value, however this can provide a metric for potentially mapping the relative packing differences across a surface. More work is needed to understand how to distinguish between the spectral slope changes due to grain-size from packing.

In the case of Ryugu, the observation that compaction creates bluer, brighter spectra suggests that the red spectral slope imply some amount of porosity to the regolith.

Surface Texture/Roughness. Binzel et al. (2015) examined the spectral properties (between 400 nm to 2500 nm) of saw-cut faces of Murchison that displayed variable amounts of surface roughness. They found the spectral slope ranged from overall blue to strongly red, suggesting that surface roughness affects spectral slope in a regolith-free environment, however they do not state if rougher surfaces are bluer or redder. Binzel et al. (2015) also examined powders of Murchison. In one case they examined a powdered sample of Murchison with a grain size of <150 μm under various particle densities and surface textures. Their conclusion was that surface texture and particle density can change the overall spectral slopes of carbonaceous chondrites, though they do not correlate specific textures and densities with bluer or redder slopes. Cloutis et al. (2018) found that surface texture had a larger affect on the photometric properties of the samples with no clear correlation with spectral slope or reddening.

Space Weathering. Laboratory experiments of 'traditional' space weathering processes (solar wind radiation and micrometeoritic bombardment) on carbonaceous asteroids show both spectral reddening and bluing (e.g. Lazzarin et al. 2006; Moroz et al. 2004; Nesvorny et al. 2005; Lantz et al. 2013, 2015, 2017; Vernazza et al. 2013; Brunetto et al. 2014; Gillis-Davis et al., 2017; Hiroi et al., 2013; Matsuoka et al. 2015, 2020, Nakamura et al., 2020; Thompson et al., 2019, 2020). A solar heating (another space weathering process) study by Hiroi et al. (1993) shows that carbonaceous chondrite samples display bluer slopes when heated. The properties of the spectral slope are ambiguous for linking traditional space-weathering processes to surface alteration, but may be indicative of heating events. More laboratory work is needed to make a definitive claim.
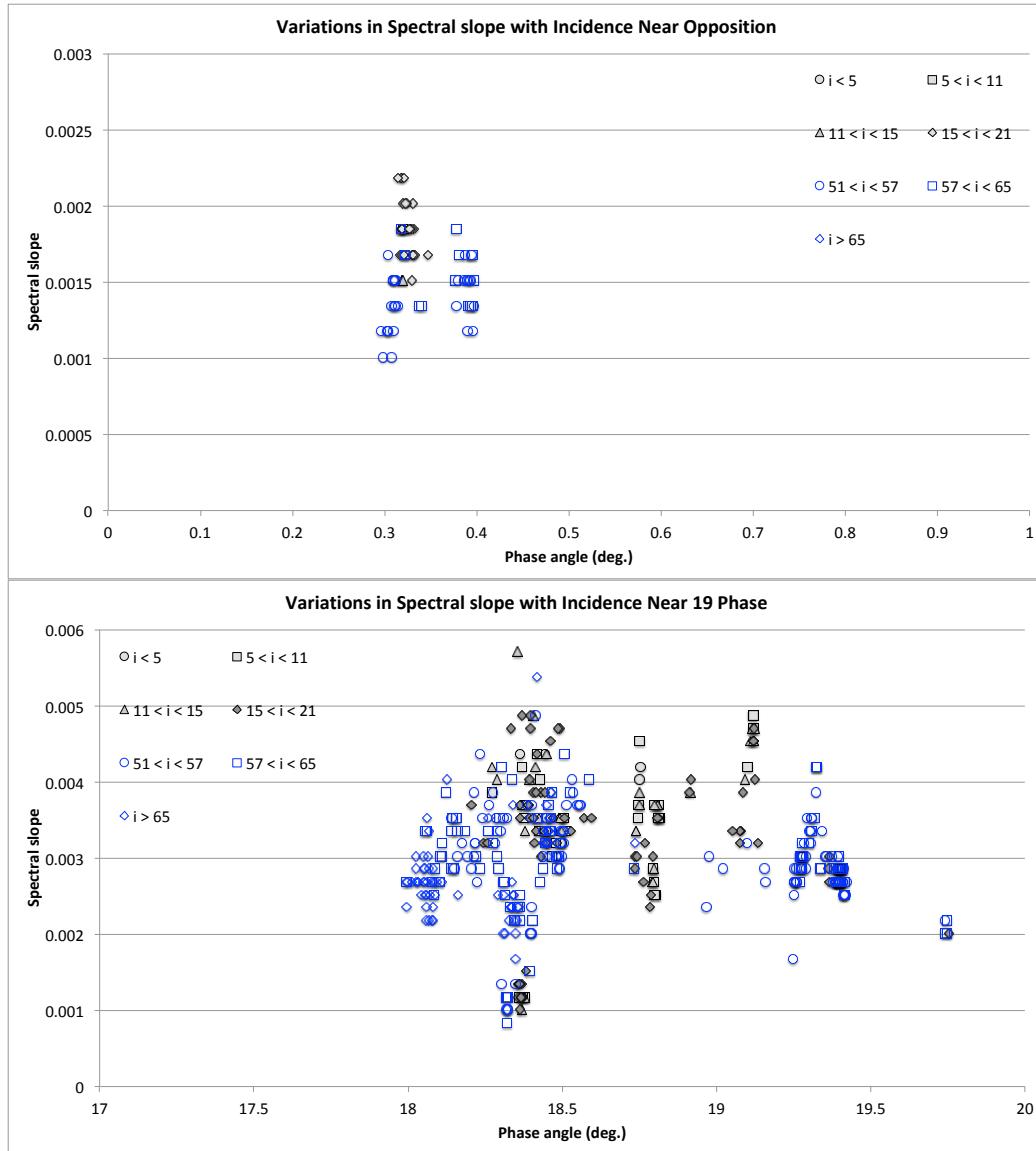
Figure 15. Comparisons of spectral slope at (top) opposition phase angles and (bottom) near 19° phase as a function of near nadir (low incidence, black symbols) and grazing (high incidence, blue symbols). No distinctive trend with incidence angle suggests the presence of a granular component at the surface of Ryugu.

The NIRS3 spectral data set can be compared with both the ONC color and ground-based observations. The normalized near-infrared observations of Moskovitz et al (2013) and Le Corre et al. (2017) are compared to a subset of the 38 – 40m footprint resolution NIRS3 opposition spectra (**Fig. 16**). All spectra are normalized to unity at 2.0 µm, and show a similar spectral shape in the wavelength range of overlap between the three data sets. Even though the spectra overlap within the noise of the ground-based observations, the NIRS3 spectra suggest a shallower slope at the longer wavelengths. The ground-based observations show differences in the spectral slope at shorter wavelengths approaching the visible and do not overlap below ~1.4µm.

21

Examination of the Moskovitz et al. (2013) normalized visible spectra, in comparison with their near-infrared spectrum (**Fig. 17**), suggests that Ryugu's spectrum is flat in the visible and increases in slope towards the near-infrared. These data have been normalized to unity at 0.86 μm. Comparison of the Moskovitz et al. (2013) visible spectra re-normalized to unity at 0.55 μm with the ONC color observations also normalized to unity at 0.55 μm demonstrates that the shape of the two spectral data sets are similar (**Fig. 17**). However, comparisons of the ONC color with the NIRS3 spectra in absolute reflectance (**Fig. 17**) shows a different relationship between the visible and near-infrared than seen in the ground-based observations, outside of what could be ascribed to differences due to phase angle variations. The visible reflectance is brighter than the near-infrared, which is opposite to the relationship seen in the Moskovitz et al. (2013) spectral observations (**Fig. 17**). The source of this spectral difference between the two instruments is currently unknown.
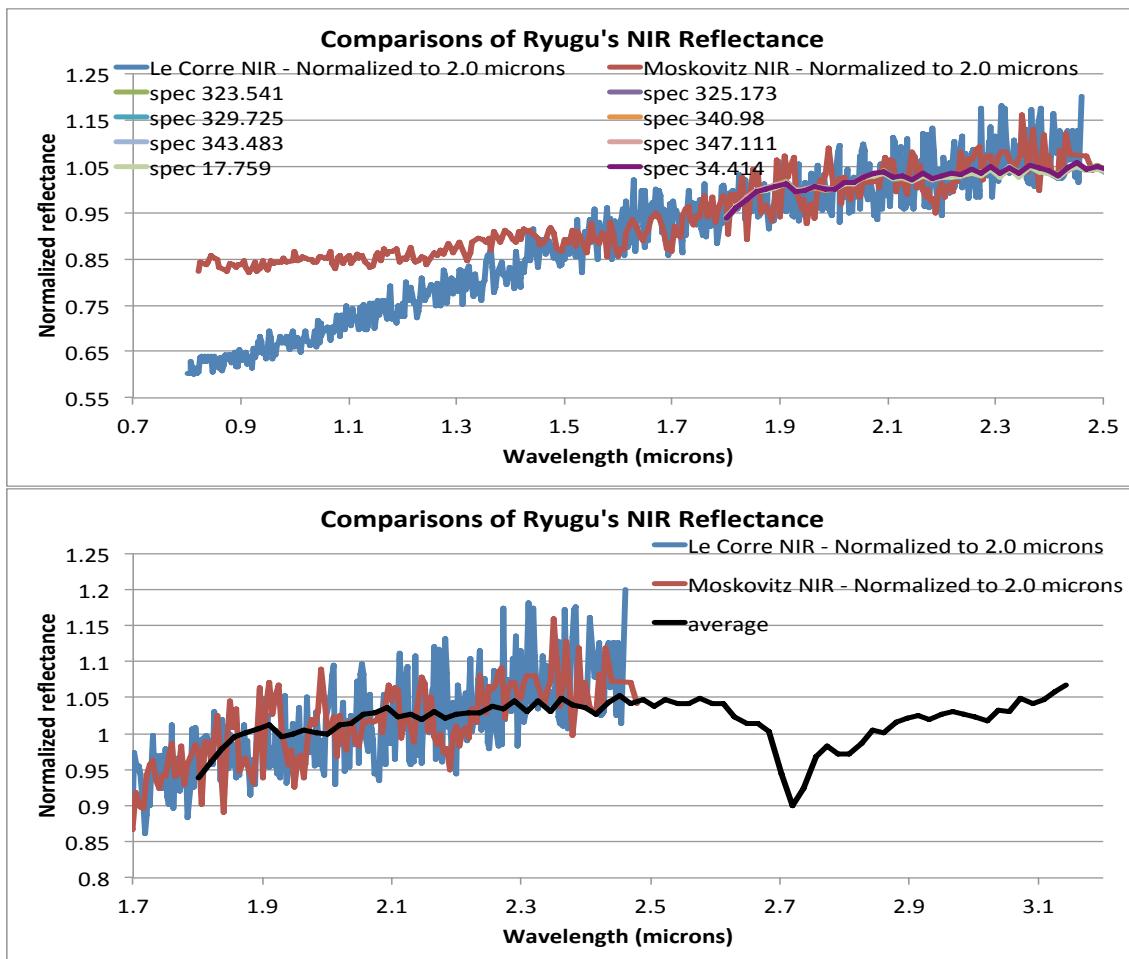
Figure 16. Example opposition spectra from the 38 – 40m footprint resolution bin across several longitudes (identified in the upper graph's legend, which overlap sufficiently that only the last spectrum, in purple, is clearly visible) from the NIRS3 data set are compared to the ground-based observations of Le Corre et al. (2017) in blue and Moskovitz et al. (2013) in red. All spectra are normalized to unity at 2.0 μm. The average of the example NIRS3 spectra is compared over the near-infrared wavelengths (bottom graph).
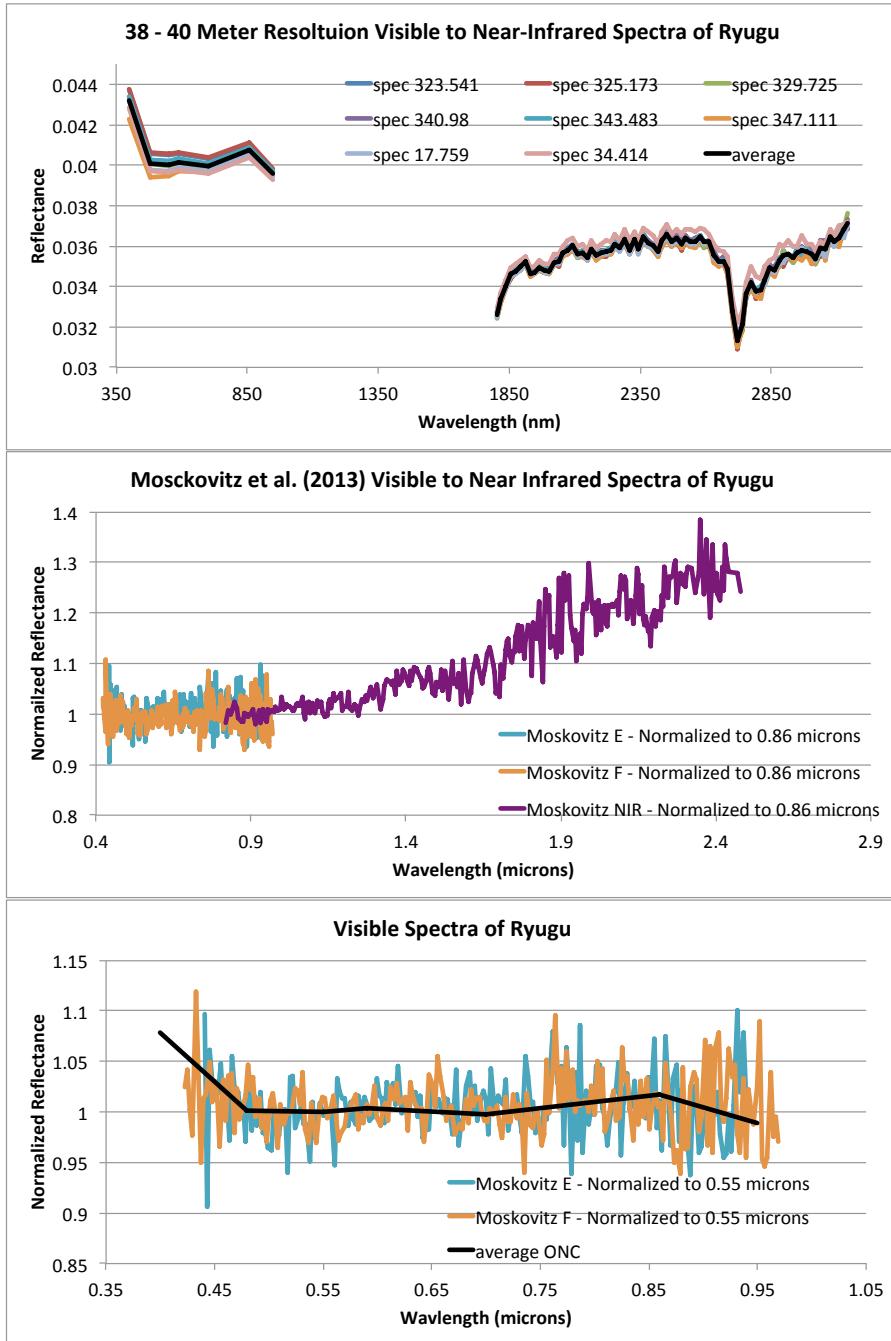
Figure 17. The observations of Moskovitz et al. (2013), shown in the center graph, display a smooth, increasing slope from the visible to the near infrared. This comparison is made be normalizing both the visible and near-infrared observations to unity at 0.86 μm. Re-normalizing the visible spectra to unity at 0.55 μm shows that the ONC color spectra display the same shape as the ground-based data (bottom graph). However, comparisons of the ONC color and NIRS3 spectra (top graph) in absolute reflectance show that the visible spectrum is brighter than the near infrared. The ONC spectra are the NIRS3 equivalent spectra derived from the normal albedo mosaics. The average spectrum shown in the top graph is the same spectrum shown in the bottom graph.

5.2 Comparisons of Photometric Properties

The ONC-T approach observations were modeled by Tatsumi et al. (2020) using the Hapke set of equations. Their results are compared to those from this study of the NIRS3 opposition data set. It is important to note that the ONC-T study included both disk-integrated and disk-resolved observations. The ONC values are derived from disk-integrated measurements constrained by disk-resolved measurements, but the NIRS3 values are derived solely from disk-resolved values. The ONC-T data set also covered a larger range of phase angle, which include disk-integrated opposition measurements. The surface roughness parameter from the ONC-T study was 28° ±6° (Tatsumi et al. 2020) whereas the NIRS3 based value is 29° ±3°, both identical within the error bars. The NIRS3 study found a uniform value of 0.318 for the single particle scattering parameter, b, whereas the ONC-T values ranged from 0.374 – 0.388 with a median value of 0.386 across all ONC-T bands (Tatsumi et al. 2020). The values correspond to a backward scattering phase function from both instrument data sets, with a more strongly backward scattering particle scattering function in the visible.

The spectral characteristics of the single scattering albedo for both instrument data sets is similar in shape to the spectral properties (**Fig. 18**). While the near-infrared spectra from the NIRS3 are darker than their counterpart visible spectra (**Fig. 17**) from the ONC-T, the opposite is seen for the single scattering albedo derived from each instrument's data set. The relative values in single scattering albedo between the visible and near-infrared are similar to what is seen in the ground-based spectral observations. The single particle scattering function is less strongly backward scattering in the NIRS3 modeling results, which results in a darker reflectance, thus the absolute reflectance differences between the visible (ONC) and near-infrared (NIRS3) is accounted for by the model in the single particle scattering function.

The opposition parameter values from the ONC-T study were assumed constant with wavelength over the instrument's band range (0.40 – 0.95 μm), since the wavelength-to-wavelength variation was minor (Tatsumi et al. 2020). The opposition parameter values from the ONC-T study are based on visible disk-integrated opposition observations, in contrast to the NIRS3 opposition data set that consists of near-infrared disk-resolved measurements. Thus the ONC parameters describe the globally averaged surface, whereas the NIRS3 parameters describe the near equatorial region they observe. The disk-resolved opposition observations from the NIRS3 data show that in the near-infrared there are variations with wavelength (**Fig. 18**). The variations in the opposition parameters derived from the NIRS3 data appear to be centered about the 2.7 μm feature, and may be due to differences caused by the material creating this absorption. This is discussed in more depth in Section 6.
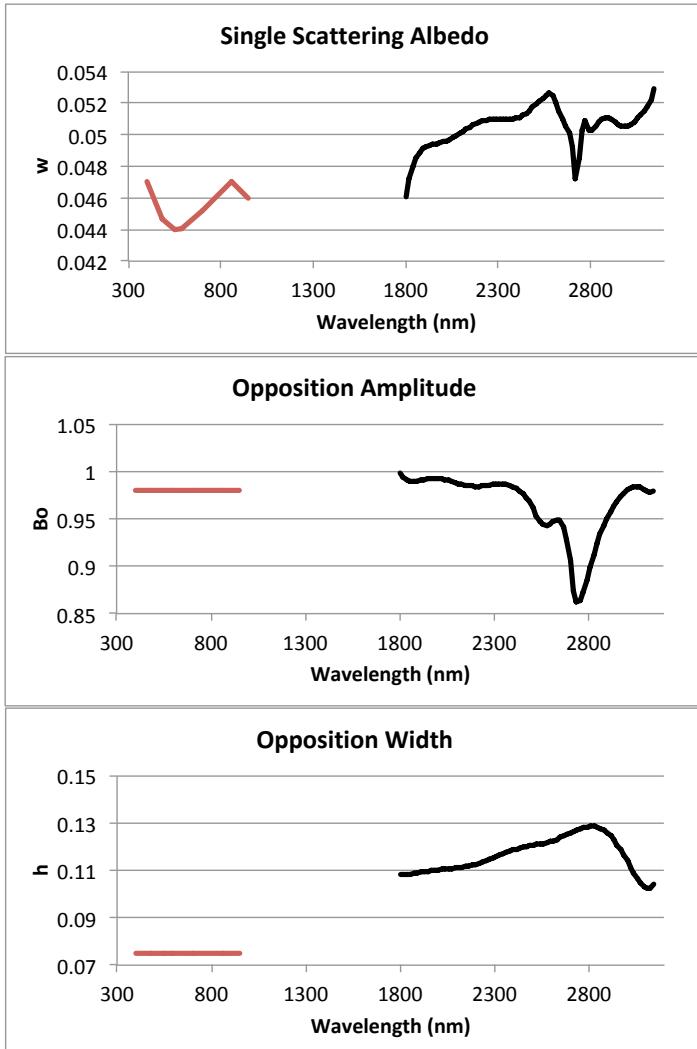
Figure 18. Comparisons of the wavelength variability of the Hapke model parameter values from the ONC-T study (Tatsumi et al. 2020) with those acquired in this study for the NIRS3 opposition data. The black lines are the NIRS3 values and the red lines are the ONC-T values. Note that the opposition parameters from the ONC-T study were set to be constant over wavelength.

6.0 Regolith Characteristics

When examining or extrapolating regolith characteristics from photometric modeling results it is important to note that the portion of the regolith that is under scrutiny is the optically active portion. This is the top layer of the regolith that interacts with the incident and subsequently reflected light. The depth within the regolith this corresponds to is dependent on the opacity and scattering efficiencies of the regolith materials, but for visible and near-infrared wavelengths this typically corresponds to the upper hundreds of micrometers. Given Ryugu's highly absorbing regolith (it is among one of the darkest objects observed), sunlight will not penetrate beyond a few tens of wavelengths. Within absorption features, such as the 2.7 μm band, the absorption coefficient increases and this can significantly reduce the penetration depth of incident photons. This section of the regolith that interacts with the incident sunlight is the portion of the regolith

we can characterize using photometric modeling. We cannot state what the properties of the regolith are at depths below a few tens of micrometers, based solely on photometric behavior.

Several photometric models, and variations on these models, have been used to study reflectance from planetary surfaces as a function of illumination and viewing geometry. One of the most common models currently in use is that derived by B. Hapke (Hapke, 1981, 1984, 1986, 1993, 2002, 2008, 2012), which is based on geometric optics and the equations of radiative transfer. It incorporates expressions and parameters to account for surface roughness, grain size and compaction, and grain scattering properties. The parameters in this model are derived to correlate to specific surface properties or sets of properties. However, many of these derivations have built in assumptions regarding the scattering surface. Laboratory tests of the correlation between Hapke model parameters with sample characteristics have shown evidence that the Hapke model parameters can be *qualitatively* related to physical properties (Shepard and Helfenstein 2007, Helfenstein and Shepard 2011, Souchon et al. 2011) and that the parameter values are often influenced by more than one property (Shepard and Helfenstein 2007). A *quantitative* correlation with regolith properties has yet to be firmly established in the laboratory.

Therefore, the first step for understanding the opposition parameters is to understand the mechanisms that produce this surge in brightness at phase angles smaller than 5°. A concise description of these mechanisms is given in Schroder et al. (2018), and is summarized here. The two dominant mechanisms contributing to the opposition effect are shadow hiding (SHOE) and coherent backscatter (CBOE). SHOE occurs when the illumination source (the Sun) is directly behind the detector/observer (in this case the spacecraft) and areas that would be in shadow are now illuminated. The resulting effect is to increase the reflectance from the surface (Hapke 1984, 1986; Shkuratov et al. 1994; Shkuratov and Helfenstein 2001). CBOE occurs through the constructive interference of light at very small phase angles (Mishechenko and Dlugach 1993; Mishchendo et al. 2009; Dlugach and Mishchenko 2013), and in order to be observed regolith grains with sizes on the order of the wavelength (in this case approximately 1 to 4 μm) are required (Mishchenko and Dlugach 1993, Schroder et al. 2018). Coherent backscatter contributes to the opposition surge for atmosphereless bright bodies, however this contribution is considered negligible for dark objects (Shevchenko and Belskaya 2010; Shevchenko et al. 2012). In the modeling presented here we consider only a shadow-hiding component to the opposition effect.

The second step for interpreting the opposition parameters is to understand their definitions and the assumptions inherent in their definitions. The opposition amplitude is defined as the amount of light from the first reflection ratioed to the total reflection at $\alpha = 0$. Based on the definition of B_o, changes in the opposition amplitude correspond to changes in the amount of light initially scattered versus the amount of light totally scattered into the opposition direction. A value of $B_o=1$ can then be interpreted as all the light is scattered from the first reflection into the opposition direction. Decreases in B_o correspond to an increase in the mechanisms that decrease the amount of light initially scattered, or an increase in absorption or transmission of light as opposed to reflection. The general correspondence of the decrease in B_o with the 2.7μm absorption feature is commensurate with these mechanisms (less light is reflected, more light is absorbed). The additional wavelength structure in B_o implies that the optical properties of the material within Ryugu's regolith are more complex than what is seen in the spectral reflectance alone. Thus the variations in the opposition surge amplitude with wavelength are attributable to the physical properties of the regolith and not simply the albedo of the regolith.

The opposition width parameter's value, based on the Hapke model derivation, is related to the porosity and grain size distribution within the optically active portion of the regolith. Hapke (2012) defines the half-width at half-maximum of the shadow-hiding opposition surge, h, as

$$h = \frac{KEa_E}{2}$$

where K is the porosity coefficient, E is the volume-averaged extinction coefficient, and a_E is the mean extinction radius (the radius of an equivalent sphere having a cross-sectional area equal to σ_E, the volume-average extinction cross-section). The porosity of the optically active portion of the regolith is wavelength invariant. However, the extinction coefficient and cross-section are dependent on the composition and physical structure of the grains within the regolith, and can vary with wavelength.

Hapke (2012) argues that if the particles are larger than the wavelength of observation and equant, and the particle size distribution is narrow, then the volume-average extinction efficiency can be assumed to be approximately unity, a_E is approximately equal to the particle radius (a), and σ_E is $\cong \pi a^2$. In this case, the opposition width, h, is related to porosity and grain size by

$$h = -\left(\frac{3}{8}\right) Y ln(\rho)$$

where ρ is the porosity and Y is the grain size distribution function which is related to the power law index β of the differential size distribution of grains (ratio of radius of the largest to smallest grain size). These assumptions imply no wavelength dependent variations in the extinction properties of the regolith material, thus the opposition parameters would be constant as a function of wavelength. This is clearly not the case for Ryugu in the near-infrared. The wavelength dependence seen in the opposition parameter values implies one or more of the above assumptions do not apply to Ryugu's regolith. Therefore the variations in the opposition surge width with wavelength are also attributable to the physical properties of the regolith and not simply the regolith's albedo.

The values of both B_o and h support wavelength dependent physical characteristics of the regolith. These characteristics include the extinction coefficient of the regolith grain material, the mean extinction radius, and that at least one of these characteristics does not apply to Ryugu's regolith: grains are larger than the observing wavelength, grains are equant, the size distribution of the grains is narrow. Based on the spectral slope and phase reddening properties, along with the imaging of the surface, the grain size distribution is neither equant or narrow, in line with the properties we see in the opposition parameters.

Comparisons of the opposition parameter values derived for Ryugu with other solar system objects (**Fig. 19 & Table 1**) allows us to make some inferences based on comparative planetology. However, the objects in **Fig. 19** (also listed in **Table 1**) were modeled using different strategies depending on the quantity and quality of the data being modeled. All objects listed, with the exception of Mathilde, are brighter than Ryugu, thus many studies include a mechanism for including a CBOE. For many of the published studies the CBOE was accounted for by allowing values of B_o to exceed unity. Those objects for which the values of B_o are ≤ 1 include Steins (Spjuth et al. 2012), Itokawa (Kitazato et al. 2008, Tatsumi et al. 2019), Eros (Clark et al. 2002, Domingue et al. 2002), Ryugu (Tatsumi et al. 2020), and the Moon (Helfenstein and Veverka,

1987), and thus provide the best comparisons with this study of Ryugu. More current lunar studies by Sato et al. (2014) allow $B_o > 1$, due to studies by Hapke et al. (1993) and Muinonen et al. (2011) which suggest that coherent backscatter plays a part in the lunar opposition surge, though this contribution to the opposition properties of the Moon has been debated (Shkuratov et al. 1999, 2012).

While it is helpful to compare Hapke model opposition parameters of one object to another, some caveats do apply. Are the parameters derived from examining observations acquired at the same wavelength? As mentioned above, there are certain physical constraints within the regolith that must be met for the opposition to be wavelength independent. Ryugu does not meet those constraints. Did the model applied incorporate the same single particle scattering function? Not all studies constrain the single particle scattering properties in the same manner. The choice is often based on the phase angle coverage within the dataset being modeled. For example, this study used a single term function that allows either forward or backward scattering, but not both simultaneously. This is because the data set itself does not sample the forward scattering direction. In contrast the studies of Eros (Clark et al. 2002; Domingue et al. 2002) utilized two-term single particle scattering functions that allow for combinations of forward and backward scattering. The single particle scattering function can affect the reflectance observed in the opposition region ($\alpha < 5°$), oft-times in subtle ways especially if the data set is limited in geometric angle coverage.

Comparisons of Ryugu's opposition parameter values (**Fig. 19**) with those from studies of other solar system objects show that, in general, Ryugu's opposition width is broader but its amplitude overlaps with the opposition characteristics of Eros, Itokawa, and some early studies of the lunar surface. The values shown for comparison are predominately from visible wavelength observations, whereas the NIRS3 results are from near-infrared observations. The different wavelength regions could be a contributor to the differences seen between Ryugu and these other objects. The ONC-T visible observations for Ryugu shown (Tatsumi et al. 2020) are closer to those for Itokawa and Helfenstein and Veverka's (1987) study of the Moon. The opposition amplitude is identical between Ryugu and Itokawa in the visible. Comparisons of Ryugu in the visible and the near-infrared show the amplitude is similar but the opposition width is broader in the near-infrared.

Near-infrared modeling results for Eros (Clark et al. 2002) and Itokawa (Kitazato et al. 2008) show the same relationship with the Ryugu results as the visible wavelength studies: overlapping amplitude values and wider width values for Ryugu. One physical parameter of the regolith that could produce this difference is a higher porosity coefficient for Ryugu compared to either Eros or Itokawa. Variations in the extinction properties, with Ryugu having either a higher extinction coefficient or extinction radius for the constituent grains in its regolith, could also explain the difference. The much darker albedo of Ryugu's regolith is commensurate with higher extinction coefficient or extinction radius values than those for either Eros or Itokawa.

Table 1. Comparisons of Opposition Parameter Values*

Asteroid	Taxonomy (system)	Bo	h	Reference
162173 Ryugu	Cb/Cg (Binzel/)	0.98 ± 0.02	0.075 ± 0.008	Tatsumi et al. 2020
25143 Itokawa	S(IV) (Tholen)	0.98 ± 0.06	0.05 ± 0.02	Tatsumi et al. 2018

|				
25143 Itokawa	S(IV) (Tholen)	0.02 ± 0.1	0.141 ± 0.1	Lederer et al. 2008
25143 Itokawa	S(IV) (Tholen)	0.867 − 0.872 ± 0.013[§]	0.006 − 0.083 ± 0.031[§]	Kitazato et al. 2008
433 Eros	S/Sw (Tholen/Bus Demeo)	1.00 ± 0.14	0.022 ± 0.005	Clark et al. 2002
433 Eros	S/Sw (Tholen/Bus Demeo)	1 ± 0.02	0.022 ± 0.005	Domingue et al. 2002
433 Eros	S/Sw (Tholen/Bus Demeo)	1.4 ± 0.1	0.010 ± 0.004	Li et al. 2004
253 Mathilde	Cb (Bus)	3.18	0.074	Clark et al. 1999
951 Gaspra	S (Tholen)	1.63 ± 0.07	0.06 ± 0.01	Helfenstein et al. 1994
243 Ida	S/Sw (Tholen/Bus Demeo)	1.53 ± 0.01	0.02 ± 0.005	Helfenstein et al. 1996
2867 Steins	E	0.60 ± 0.05	0.027 ± 0.002	Spjuth et al. 2012
21 Lutetia	M/Xc (Tholen/Bus Demeo)	[1.79]	[0.041]	Masoumzadeh et al. 2015 Hasselmann et al. 2016
4 Vesta	V (Tholen/Bus Demeo)	1.66	0.076	Li et al. 2013
1 Ceres	G/C (Tholen/Bus Demeo)	3.1	0.081	Schroder et al. 2018
		1.8	0.056	
		1.6	0.054	
67P/CG	Comet	2.42 ± 0.3	0.081 ± 0.005	Hasselmann et al. 2017
Moon		0.71	0.07	Helfenstein & Veverka (1987)
Moon (average)		2.01	0.079	Sato et al. (2014)
Moon (highlands)		2.09	0.073	Sato et al. (2014)
Moon (mare)		2.52	0.053	Sato et al. (2014)
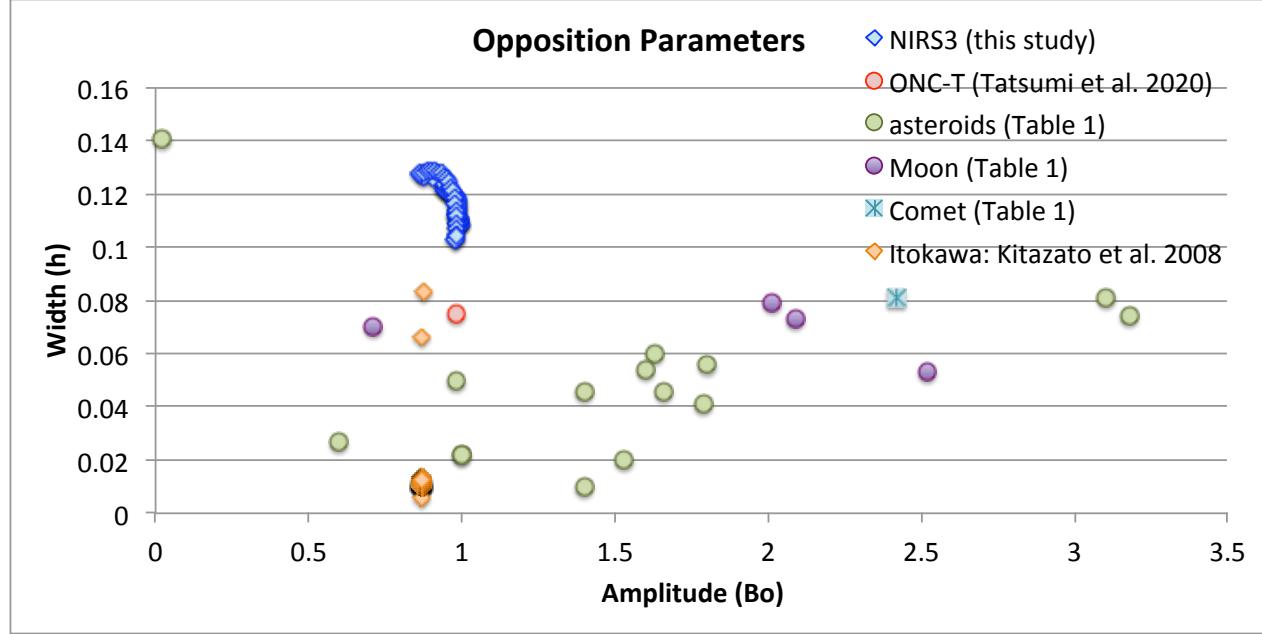
Figure 19. Comparisons of the values of the opposition amplitude (Bo) with the opposition width (h) for several solar system objects. The Ryugu values from this study (blue diamonds) are plotted with those from the ONC-T (red circle), those from other asteroids (green circles), the Moon (purple circles), and comet 67P/CG (blue asterisk). The values from the near-infrared study of Itokawa by Kitazato et al. (2008, orange diamonds) are also shown. Table 1 shows the values for the specific objects that are being compared with the NIRS3 derived parameter values. NOTE: the comparison is being made between the NIRS3 near-infrared values with visible wavelength values of other objects, with the exception of the modeling results of Itokawa by Kitazto et al. (2008).

Another method for characterizing the opposition surge is to examine and compare the reflectance at 0.3° phase with the reflectance at 5° phase. Belskaya and Shevchenko (2000) examine the ratio of the reflectance at these two phase angles for several asteroids observed in the visible at 0.55 μm (see Belskaya and Shevchenko (2000) Table 1). A plot of the geometric albedo versus this opposition ratio (**Fig. 21**) is compared with values from Tatsumi et al. (2020) from the observations at 0.55 μm (v-band) and those from this study at 2.0 μm and 2.7 μm. We used the geometric albedo at 0.55 μm derived by Tatsumi et al. (2020) of 0.04 ± 0.005 and use their Hapke parameter values to derive the reflectance of Ryugu at 0.3° and 5.0° phase to calculate the ratio. The v-band value for Ryugu plots within the grouping for C-, F- and P-class asteroids in the ECAS taxonomy.

The near-infrared ratio values were derived from the 38 – 40 m data observations. All observations within $0.3° \pm 0.005°$ were averaged together to provide the reflectance value at 0.3° phase. All observations within $5.0° \pm 0.005°$ were averaged together to provide the reflectance

value at 5.0° phase. The ratio was then calculated for each wavelength (**Fig. 21**). The geometric albedos at 2.0 μm and 2.7 μm were derived using the Hapke model and the model parameter values for those wavelengths. The values at 2.0 μm and 2.7 μm are compared with the 550 nm values. The near-infrared ratios are much lower than their visible counterparts and the geometric albedo values at 2.0 μm and 2.7 μm (0.035 and 0.033, respectively) are significantly darker than the value at 0.55 μm. The properties of Ryugu's opposition in the near-infrared is clearly different than those for other objects observed in the visible.

The opposition ratio for Ryugu also shows a strong variation with wavelength, as is seen in the Hapke modeling results. This variation with wavelength supports the finding from the modeling that the opposition is not only dependent on the albedo of the surface, but is influenced by the physical structure of the regolith.
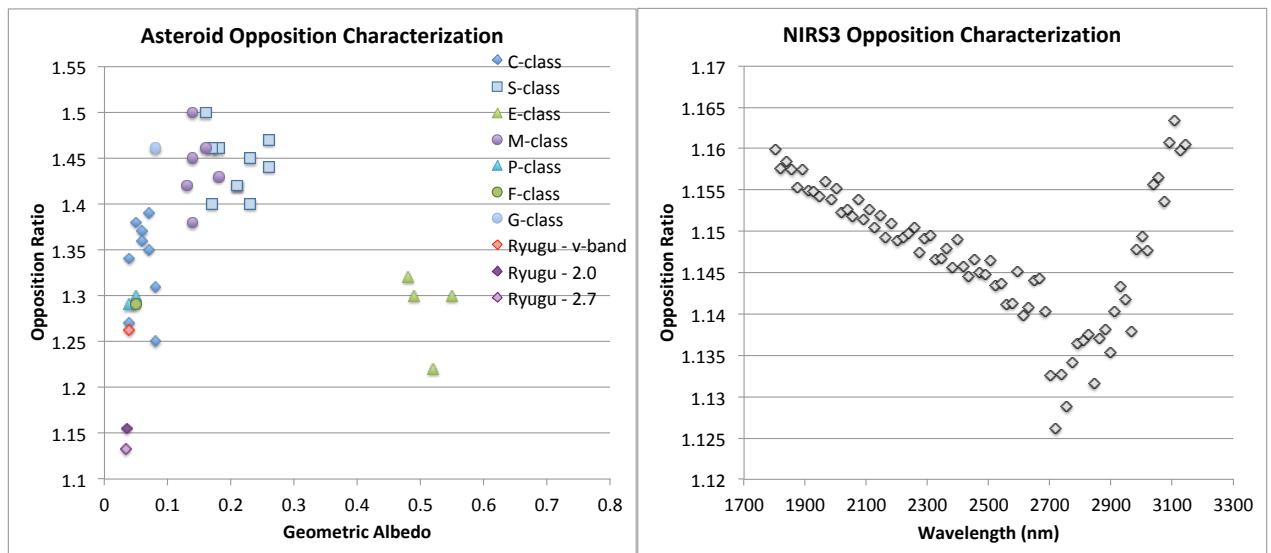

Figure 20. (left) Comparisons of the opposition ratio (reflectance at 0.3° phase/reflectance at 5.0° phase) with the asteroid data set from Belskaya and Shevchenko (2000). (right) Variations in the opposition ratio with wavelength for the near-infrared, as derived from the NIRS3 38 − 40m observations.

7.0 Discussion/Conclusions

This study of Ryugu's opposition surge in the near-infrared provides some additional insight into the properties of the optically active portion of its regolith. Unlike the photometric behavior observed in the visible, which shows the opposition model parameters to be uniform with wavelength (Tatsumi et al. 2020), the opposition parameters in the near-infrared show a clear variation with wavelength. The variation in both amplitude and width are commensurate with wavelength dependencies in the absorption and physical properties (particle shape and distribution of sizes) of the regolith material. While the near-infrared spectra acquired by the NIRS3 instrument display a very dark, flat spectrum with a single sharp absorption at 2.7 μm, the photometry shows broader variations in the opposition parameters, with a maximum near 2.74 μm and 2.8 μm, for B_o and h, respectively. Based on the Hapke model derivation and definitions of the opposition parameters, the wavelength dependence of both the opposition amplitude and width are attributable to the physical properties (such as absorption properties, particle shape, and

31

grain size distribution) of the regolith and not only the regolith's albedo. This is also supported by the opposition ratio properties.

The wavelength variation in the opposition amplitude can be ascribed to either (or both) the composition of the regolith or the nature of the scattering centers within the regolith grains. The nature of the scattering centers is to reflect the incident light such that it does not return directly to the detector and is multiply scattered such that it is lost to detection. This can be accomplished via composition (highly absorbing media), particle inclusions, or particle shape. Ryugu's dark regolith is composed of highly absorbing material, thus making it difficult to discern the role of the regolith particle characteristics solely based on the opposition amplitude.

The opposition width wavelength characteristics argue that one or more of the following characteristics are invalid for describing Ryugu's regolith: (1) regolith grains/particles are larger than the wavelength of light, (2) these grains/particles are equant, and (3) the grain/particle size distribution is narrow. ONC images of Ryugu's surface boulders (Fig. 22) shown by Sugita et al. (2019) clearly show the presence of a granular component to Ryugu's surface, even though it may not completely cover the entire surface. ONC images acquired at ~42 m altitude show regions on the surface containing particles several cm in size (Sakatani et al. 2019). The MASCOT lander studies do not show any evidence for fine-grained dust (Jaumann et al. 2019; Grott et al. 2019; Biele et al. 2019). However, thermal studies suggest that the boulders on Ryugu are highly porous (Okada et al., 2020; Shimaki et al. 2020). The thermal inertia properties show that Ryugu's boulders are consistent with a fragile porous matrix that is easily disrupted to produce fine-grains (Okada et al., 2020; Shimaki et al. 2020). These fine-grains could accumulate on the surface to mix with the coarser-grained regolith, or even coat the coarser grains, apparent in the images. Observations of particles elevated by the thrusting during the Touch Down 1 (TD1) operations (Morota et al. 2020; Tsuda et al. 2020) along with the thermal inertia measurements (Shimaki et al. 2020) suggest that fine-grains exist in some regions as a portion of Ryugu's regolith. This is commensurate with the photometric behavior of the spectral slope we observe in the NIRS3 data set. The phase reddening behavior with both phase and incidence angle, in comparison with laboratory measurements of carbonaceous meteorites, indicate a granular regolith with a fine-grained ($< 45\mu m$) component.

In December 2020 the samples collected from Ryugu's surface will be returned to Earth. The mystery of the regolith grain size distribution may be revealed in the sample capsule.
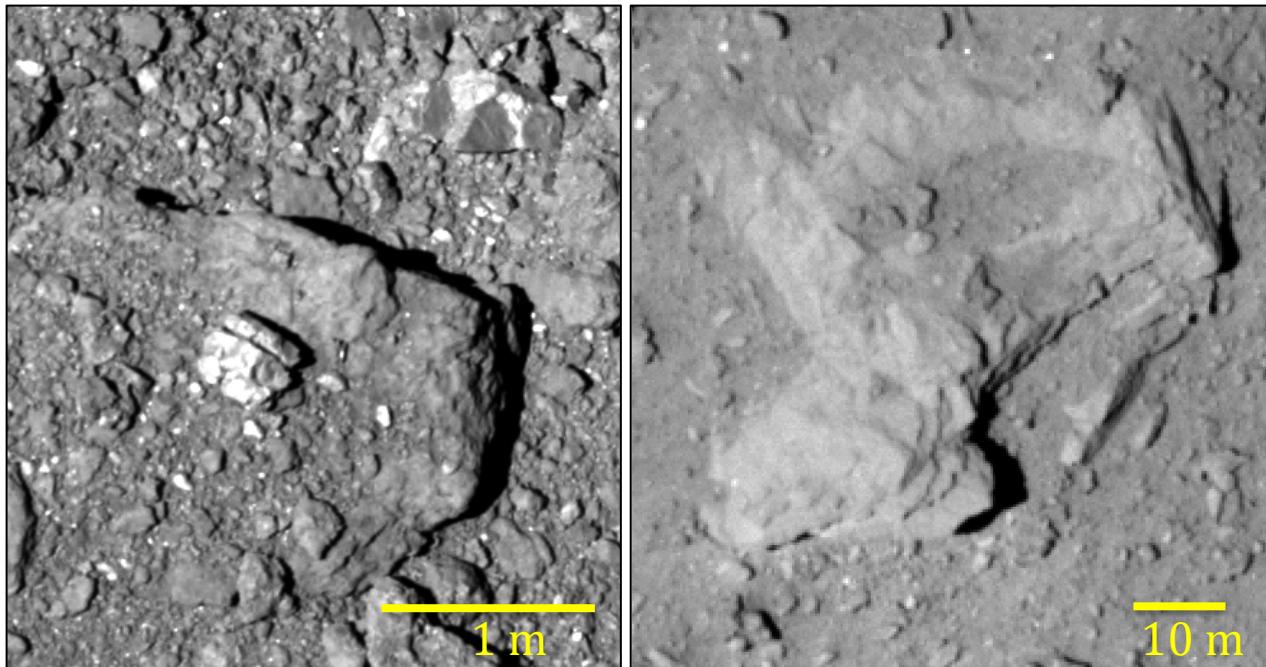
Figure 21. (left) A boulder near the MINERVA-II landing site partially covered with regolith. (right) Type 2 boulder displaying some coverage by regolith. Coarse-grained (mm – cm) regolith is apparent at the resolution of both these images

References

Barucci, M.A., Hasselmann, P.H., Fulchignoni, M., Honda, R., Yokota, Y., Sugita, S., Kitazato, K., Deshapriya, J.D.P., Perna, D., Tatsumi, E., Domingue, D., Morota, T., Kameda, S., Iwata, T., Abe, M., Ohtake, M., Matsuura, S., Matsuoka, M., Hiroi, T., Nakamura, T., Kouyama, T., Suzuki, H., Yamada, M., Sakatani, N., Honda, C., Ogawa, K., Hayakawa, M., Yoshioka, K., Cho, Y., Sawada, H., Takir, D., Vilas, F., Hirata, N., Hirata, N., Tanaka, S., Yamamoto, Y., Yoshikawa, M., Watanabe, S., Tsuda, Y., 2019. Multivariable statistical analysis of spectrophotometry and spectra of (162173) Ryugu as observed by JAXA Hayabusa2 mission. A&A 629, doi:10.1051/0004-6361/201935851

Beck, P., Pommerol, A., Thomas, N., Schmitt, B., Moynier, F., Barrat, J.-A., 20112. Photometry of meteorites, Icarus, 218, 364 – 377, doi:10.1016/j.icarus.2011.12.005.

Belskaya, I.N. and Shevchenko, V.G., 2000. Opposition effect of asteroids. Icarus 147 (1), 94–105. https://doi.org/10.1006/icar.2000.6410.

Biele, J., Kührt, E., Senshu, H., Sakatani, N., Ogawa, K., Hamm, M., Grott, M., Okada, T., Arai, T., 2019. Effects of dust layers on thermal emission from airless bodies. Progress in Earth and Planetary Science, 6, 48.

Binzel, R.P., DeMeo, F.E., Burt, B.J., Cloutis, E.A., Rozitis, B., Burbine, T.H., Campins, H., Clark, B.E., Emery, J.P., Hergenrother, C.W., Howell, E.S., Lauretta, D.S., Nolan, M.C., Mansfield, M., Pietrasz, V., Polishook, D., Scheeres, D.J., 2015. Spectral slope variations for OSIRIS-REx target Asteroid (101955) Bennu: Possible evidence for a fine-grained regolith equatorial ridge. Icarus 256, 22 – 29, doi:10.1016/j.icarus.2015.04.011

Brunetto, R., Lantz, C., Ledu, D., Baklouti, D., Barucci, M.A., Beck, P., Delauche, L., Dionnet, Z., Dumas, P., Duprat, J., Engrand, C., Jamme, F., Oudayer, P., Quirico, E., Sandt, C., Dartois, E., 2014. Ion irradiation of Allende meteorite probed by visible, IR, and Raman spectroscopies. Icarue 237, 278 – 292. doi: 10.1016/j.icarus.2014.04.047

Clark, B.E., Veverka, J., Helfenstein, P., Thomas, P.C., Bell III, J.F., Harch, A., 1999. NEAR Photometry of Asteroid 253 Mathidle. Icarus 140, 53 – 65.

Clark, B. E., Helfenstein, P., Bell, J.F., Peterson, C., Veverka, J., Izenberg, N. I., Domingue, D., Wellnitz, D., McFadden, L. (2002). NEAR Infrared Spectrometer Photometry of Asteroid 433 Eros, Icarus 155, Issue 1, 189-204, ISSN 0019-1035, doi:10.1006/icar.2001.6748.

Cloutis, E.A., Hudon, P., Hiroi, T., Gaffey, M.J., Mann, P., 2011. Spectral reflectance properties of carbonaceous chondrites: 1. CM chondrites. Icarus 216, 309 – 346, doi:10.1016/j.icarus.2011.09.009

Cloutis, E.A., Hudon, P., Hiroi, T., Gaffey, M.J., Mann, P., Alexander, C.M. O'D., Bell, J.F., Clark, B.E., 2013. Possible causes of blue slopes (0.5–2.5 lm) in carbonaceous chondrite spectra. Lunar Planet. Sci. 44, no. 1719, 1550.

Cloutis, E. A. et al. Spectral reflectance "deconstruction" of the Murchison CM2 carbonaceous chondrite and implications for spectroscopic investigations of dark asteroids. *Icarus* 305, 203-224 (2018).

Dlugach, Zh. M., Mishchenko, M.I., 2013. Coherent backscattering and opposition effects observed in some atmosphereless bodies of the solar system. *Sol Syst Res* **47,** 454–462 (2013). https://doi.org/10.1134/S0038094613060014

Domingue, D.L., Murchie, S.L., Denevi, B.W., Ernst, C.M., Chabot, N.L., 2015. Mercury's global color mosaic: An update from MESSENGER's orbital observations. Icarus 257, 477 – 488.

Domingue, D.L., Denevi, B.W., Murchie, S.L., Hash, C.D. 2016a. Application of multiple photometric models to disk-resolved measurements of Mercury's surface: Insights into Mercury's regolith characteristics. Icarus 268, 172 – 203.

Domingue, D.L., Vilas, F., Choo, T., Stockstill-Cahill, K.R., Cahill, J.T.S., Hendrix, A.R., 2016b. Regional spectrophotometric properties of 951 Gaspra. Icarus 280, 340 – 358, doi:10.1016/j.icarus.2016.07.011.

Domingue, D., Palmer, E., Gaskell, R., Staid, M. 2018. Characterization of lunar surface within Tsiolkovsky crater: Photometric properties. Icarus 312, 61 -99.

Domingue, D., M. Robinson, B. Carcich, J. Joseph, P. Thomas, and B. E. Clark 2002. Disk-integrated photometry of 433 Eros. Icarus 155, 205 – 219.

Gillis-Davis, J.J., Lucey, P.G., Bradley, J.P., Ishii, H.A., Connolly, H.C., 2013. Laser space weathering of Allende meteorite. Lunar Planet. Sci. 44, no. 1719, 2494.

Gillis-Davis, J. J., Lucey, P. G., Bradley, J. P., Ishii, H.A., Kaluna, H.M., Misra, A., Connolly Jr., H.C., 2017, Incremental laser space weathering of Allende reveals non-lunar like space weathering effects. Icarus 286, 1 – 14, doi:10.1016/j.icarus.2016.12.031

Gradie, J., Veverka, J., Buratti, B., 1980. The effects of scattering geometry on the spectrophotometric properties of powdered material. Proc. 11th Lunar and Planet. Sci. Conf. 357–359.

Gradie, J., Veverka, J., 1986. The wavelength dependence of phase coefficients. Icarus 66,455–467.

Grott, M., Knollenberg, J., Hamm, M., Ogawa, K., Jaumann, R., Otto, K.A., Delbo, M., Michel, P., Biele, J., Neumann, W., Knapmeyer, M., Kuhrt, E., Senshu, H.,, Okada, T., Helbert, J., Maturilli, A., Muller, N., Hagermann, A., Sakatani, N., Tanaka, S., Arai, T., Mottola, S., Tachibana, S., Pelivan, I., Drube, L., Vincent, J.-B., Yano, H., Pilorget, C., Matz, C., Schmitz, N., Koncz, A., Schroder, S.E., Trauthan, F., Schlotterer, M., Krause, C., Ho, T.-M., Moussi-Soffys, A., 2019. Nature Astronomy, doi:10.1038/s41550-019-0832-x

Hapke, B., 1981. Bidirectional reflectance spectroscopy. 1. Theory. J. Geophys. Res. 68, 4571 – 4586.

Hapke, B., 1984. Bidirectional reflectance spectroscopy 3. Correction for macroscopic roughness. Icarus 59, 41 – 59.

Hapke, B., 1986. Bidirectional reflectance spectroscopy 4. The extinction coefficient and the opposition effect. Icarus 67, 264 – 280.

Hapke, B. W., Nelson, R. M., Smythe, W. D., 1993. The opposition effect of the moon: the contribution of coherent backscatter. Science, 260(5107), 509-511.

Hapke, B., 2002. Bidirectional reflectance spectroscopy. 5. The coherent backscatter opposition effect and anisotropic scattering. Icarus 157, 523 – 534.

Hapke, B., 2008. Bidirectional reflectance spectroscopy. 6. Effects of porosity. Icarus 195, 918 – 926.

Hapke, B., 2012a. Theory of Reflectance and Emittance Spectroscopy. Cambridge University Press, NY, 2nd Edition, 513 pp.

Hasselmann, P.H., Barucci, M.A., Fornasier, Leyrat, C., Carvano, J.M., Lazzaro, D., Sierks, H., 2016. Asteroid (21) Lutetia: Disk-resolved photometric analysis of Baetica region. Icarus 267, 135 – 153, doi:10.1016/j.icarus.2015.11.023

Hasselmann, P.H., Barucci, M.A., Fornasier, S., Feller, C., Deshapriya, j.D.P., Fulchignoni, M., Jost, B., Sierks, H., Barbieri, C., Lamy, P.L., Rodrigo, R., Koschny, D., Rickman, H., A'Hearn, M., Bertaux, J.-L., Bertini, I., Cremonese, G., Da Deppo, V., Davidsson, B., Debei, S., De Cecco, M., Deller, J., Fulle, M., Gaskell, R.W., Groussin, O., Gutierrez, P.J., Guttler, C., Hofmann, M., Hviid, S.F., Ip, W.-H., Jorda, L., Keller, h.U., Knollenberg, J., Kovacs, G., Kramm, R., Kuhrt, E., Kuppers, M., Lara, M.L., Lazzarin, M., Lopez-Moreno, J.J., Marzari, F., Mottola, S., Naletto, G., Oklay, N., Pommerol, A., Thomas, N., Tubiana, C., Vincent, J.-B., 2017. The opposition effect of 67P/Churyumov-Gerasimenko on post-perihelion Rosetta images. Monthly Notices of the Royal Astronomical Society, 469, Issue Supp. 2, S550 – S567.

Helfenstein, P., J. Veverka 1987. Photometric properties of lunar terrans derived from Hapke's equation. Icarus 72, 342 – 357.

Helfenstein, P., Veverka, J., Thomas, P.C., Simonelli, D.P., Lee, P., Klaasen, K, Johnson, T.V., Breneman, H., Head, J.W., Murchie, S., 1994. Galileo photometry of Asteroid 951 Gaspra, Icarus, 107, 37 – 60.

Helfenstein, P., Veverka, J., Thomas, P.C., Simonelli, D.P., Klaasen, K., Johnson, T.V., Fanale, F., Granahan, J., McEwen, A.S., Belton, M., Chapman, C, 1996. Galileo photometry of Asteroid 243 Ida, Icarus, 120, 48 – 65.

Helfenstein, P., Shepard, M. K., 2011. Testing the Hapke photometric model: Improved inversion and the porosity correction. Icarus, 215(1), 83-100.

Hiroi, T., Pieters, C.M., Zolensky, M.E., Lipschutz, M.E., 1993. Evidence of thermal metamorphism on the C, G, B, and F asteroids. Science 261, 1016–1018. doi: 10.1126/science.261.5124.1016

Hiroi, T., Pieters, C.M., Zolensky, M.E., Prinz, M., 1996. Reflectance spectra (UV-3µm) of heated Ivuna (CI) meteorite and newly identified thermally metamorphosed CM chondrites. *Lunar and Planetary Science 27*, 551-552.

Hiroi, T., Sasaki, S., Misu, T., Nakamura, T., 2013. Keys to detect space weathering on Vesta: Changes of visible and near-infrared reflectance spectra of HEDs and carbonaceous chondrites. Lunar and Planetary Sci Conf. 44, no. 1719, 1276

Iwata, T., Kitazato, K., Abe, M., Ohtake, M., Arai, T., Arai, T., Hirata, N., Hiroi, T., Honda, C., Imae, N., Komatsu, M., Matsunaga, T., Matsuoka, M., Matsuura, S., Nakamura, T., Nakato, A., Nakaushi, Y., Osawa, T., Senshu, H., Takagi, Y., Tsumura, K., Takato, N., Watanabe, S.-I., Barucci. M.A., Palomba, E., Ozaki, M., 2017. NIRS3: The near infrared spectrometer on Hayabusa2. *Space Sci Rev* **208,** 317–337 (2017). https://doi.org/10.1007/s11214-017-0341-0

Jaumann, R., Schmitz, N., Ho, T.-M., Schroder, S.E., Otto, K.A., Stephan, K., Elgner, S., Krohn, K., Preusker, F., Scholten, F., Biele, J., Ulamec, S., Krause, C., Sugita, S., Matz, K.-D., Roatsch, T., Parekh, T., Mottola, S., Grott, M., Michel, P., Trauthan, F., Koncz, A., Michaelis, H., Lange, C., Grundmann, J.T., Maibaum, M., Sasaki, K., Wolff, F., Reill, J., Moussi-Soffys, A., Lorda, L., Neumann, W., Vincent, J.-B., Wagner, R., Bibring, J.-P., Kameda, S., Yano, H., Watanabe, S., Yoshikawa, M., Tsuda, Y., Okada, T., Yoshimitsu, T., Mimasu, Y., Saiki, T., Yabuta, H., Rauer, H., Honda, R., Morota, T., Yokota, Y., Kouyama, T., 2019. Images from the surface of asteroid Ryugu show rocks similar to carbonaceous chondrite meteorites. Science 365, 817 – 820.

Johnson, Torrence V., Fanale, Fraser P., 1973. Optical properties of carbonaceous chondrites and their relationship to asteroids. J. Geophys. Res. 78 (35), 8507–8518. https://doi.org/10.1029/JB078i035p08507.

Kitazato, K., Clark, B.E., Abe, M., Abe, S., Takagi, Y., Hiroi, T., Barnouin-Jha, O.S., Abell, P.A., Lederer, S.M., Vilas, F., 2008. Near-infrared spectrophotometry of Asteroid 25143 Itokawa from NIRS on the Hayabusa spacecraft. Icarus 194, 137 – 145, doi:10.1016/j.icarus.2007.08.029.

Kitazato, K., Milliken, R.E., Iwata, T., Abe, M., Ohtake, M., Matsuura, S., Arai, T., Nakauchi, Y., Nakanura, T., Matsuoka, M. Senshu, H., Hirata, N., Hiroi, T., Pilorget, C., Brunetto, R., Poulet, F., Riu, L., Bibring, J.-P., Takir, D., Domingue, D.L., Vilas, F., Barucci, M.A., Perna, D., Palomba, E., Galiano, A., Tsumura, K., Osawa, T., Komatsu, M., Nakato, A., Arai, T., Takato N., Matsunaga T., Takagi, Y., Matsumoto, K., Kouyama, T., Yokota, Y., Tatsumi, E., Sakatani, N., Yamamoto, Y., Okada, T., Sugita, S., Honda, R., Morota, T., Kameda, S., Sawada, H., Honda, C., Yamada, M., Suzuki, H., Yoshioka, K., Hayakawa, M., Ogawa, K., Cho, Y., Shirai, K., Shimaki, Y., Hirata, N., Yamaguchi, A., Ogawa, N., Terui, F., Yamaguhci, T., Takei, Y., Saikim T., Nakazawa S., Tanaka, S., Yoshikawa, M., Watanabe, S., Tsuda, Y., 2019. The surface composition of asteroid 162173 Ryugu from Hayabusa2 near-infrared spectroscopy. Science. https://doi.org/10.1126/science.aav7432. (doi:10.1126/science.aav7432).

Lantz, C., Brunetto, R., Barucci, M. A., Fornasier, S., Baklouti, D., Bourcois, J., Godard, M., 2017, Ion irradiation of carbonaceous chondrites: A new view of space weathering on primitive asteroids. Icarus, 285, 43 – 57, doi:10.1016/j.icarus.2016.12.019

Lantz, C., Brunetto, R., Barucci, M.A., Dartois, E., Duprat, J., Engrand, C., Godard, M., Ledu, D., Quirico, E., 2015. Ion irraditiaon of the Murchison meteorite: Visible to mid-infrared spectroscopic results. A&A 577, A41, doi:10.1051/0004-6361/201425398.

Lantz, C., Clark, B.E., Barucci, M.A., Lauretta, D.S., 2013. Evidence for the effects of space weathering spectral signatures on low albedo asteroids. Astron. Astrophys. 554. A138, 1–7. doi:10.1051/0004-6361/201321593

Lazzarin, M., Marchi, S., Moroz, L.V., Brunetto, R., Magrin, S., Paolicchi, P., Strazzulla, G., 2006. Space weathering in the main asteroid belt: The big picture. Astrophys. J. 647, Issue 2, L179 – L182, doi:10.1086/507448.

Le Corre, L., Sanchez, J.A., Reddy, V., Takir, D., Cloutis, E.A., Thirouin, A., Becker, K.J., Li, J.-Y., Sugita, S., Tatsumi, E., 2017. Ground-based characterization of Hayabusa2 mission target asteroid 162173 Ryugu: constraining mineralogical compositin in preparation for spacecraft operations. *Monthly Notices of the Royal Astronomical Society*, Volume 475, Issue 1, March 2018, Pages 614–623, doi:10.1093/mnras/stx3236.

Lederer, S.L., Domingue, D.L., Thomas-Osip, J.E., Vilas, F., Osip, D.J., Leeds, S.L., Jarvis K.S. 2008. The 2004 Las Campanas/Lowell Observatory campaign II. Surface properties of Hayabusa target Asteroid 25143 Itokawa inferred from Hapke modeling. Earth Planets Space 60, 49 – 59.

Li, J., A'Hearn, M. F., McFadden, L. A., 2004. Photometric analysis of Eros from NEAR data. Icarus, 172(2), pp. 415-431.

Li, J. Y., Le Corre, L., Schröder, S. E., Reddy, V., Denevi, B. W., Buratti, B. J., Mottola, S., Hoffmann, M., Gutierrez-Marques, P., Nathues, A., Russell, C. T., Raymond, C. A., 2013. Global photometric properties of Asteroid (4) Vesta observed with Dawn Framing Camera. Icarus, 226(2), pp. 1252-1274.

Masoumzadeh, N., Boehnhardt, H., Li, J.-Y., Vincent, J.-B., 2015. Photometric analysis of Asteroid (21) Lutetia from Rosetta-OSIRIS images. Icarus 257, 239 – 250.

Matsuoka, M., Nakamura, T., Kimura, Y., Hiroi, T., Nakabura, R., Okumura, S., Sasaki, S., 2015. Pulse-laser irradiation experiments of Murchison CM2 chondrite for reproducing space weathering on C-type asteroids. Icarus, 254, 135 – 143, doi: 10.1016/j.icarus.2015.02.029.

Matsuoka, M., Nakamura, T., Hiroi, T., Okumura, S., & Sasaki, S. (2020). Space Weathering Simulation with Low-energy Laser Irradiation of Murchison CM Chondrite for Reproducing Micrometeoroid Bombardments on C-type Asteroids. *The Astrophysical Journal Letters*, *890*(2), L23.

Mishchenko, M.I., and J.M. Dlugach, 1993: Coherent backscatter and the opposition effect for E-type asteroids. *Planet. Space Sci.*, **41**, 173-181, doi:10.1016/0032-0633(93)90056-8.

Mishchendo, M.I., Dlugach, J.M., Lui, L., Rosenbush, V.K., Kiselev, N.N., Shkuratov, Y.G., 2009. Direct solutions of the Maxwell equations explain opposition phenomena observed for high-albedo solar system objects. Astro. Phys. Lett. 705, Issue 2, L118 – L122. doi:10.1088/0004-637X/705/2/L188.

Morota, T., Sugita, S., Cho, Y., Kanamaru, M., Tatsumi, E., Sakatani, N., Honda, R., Hirata, N., Kikuchi, H., Yamada, M., Yokota, Y., Kameda, S., Matsuoka, M., Sawada, H., Honda, C., Kouyama, T., Ogawa, K., Suzuki, H., Yoshioka, K., Hayakawa, M., Hirata, N., Hirabayashi, M., Miyamoto, H., Michikami, T., Hiroi, T., Hemmi, R., Barnouin, O. S., Ernst, C. M., Kitazato, K., Nakamura, T., Riu, L., Senshu, H., Kobayashi, H., Sasaki, S., Komatsu, G., Tanabe, N., Fujii, Y., Irie, T., Suemitsu, M., Takaki, N., Sugimoto, C., Yumoto, K., Ishida, M., Kato, H.,

Moroi, K., Domingue, D., Michel, P., Pilorget, C., Iwata, T., Abe, M., Ohtake, M., Nakauchi, Y., Tsumura, K., Yabuta, H., Ishihara, Y., Noguchi, R., Matsumoto, K., Miura, A., Namiki, N., Tachibana, S., Arakawa, M., Ikeda, H., Wada, K., Mizuno, T., Hirose, C., Hosoda, S., Mori, O., Shimada, T., Soldini, S., Tsukizaki, R., Yano, H., Ozaki, M., Takeuchi, H., Yamamoto, Y., Okada, T., Shimaki, Y., Shirai, K., Iijima, Y., Noda, H., Kikuchi, S., Yamaguchi, T., Ogawa, N., Ono, G., Mimasu, Y., Yoshikawa, K., Takahashi, T., Takei, Y., Fujii, A., Nakazawa, S., Terui, F., Tanaka, S., Yoshikawa, M., Saiki, T., Watanabe, S., Tsuda, Y., 2020. Sample collection from asteroid (162173) Ryugu by Hayabusa2: Implications for surface evolution. Science 368, Issue 6491, 654 – 659, doi:10.1126/science.aaz63063

Moroz, L.V., Hiroi, T., Shingareva, T.V., Basilevsky, a.T., Fisenko, A.V., Semjonova, L.F., Pieters, C.M., 2004. Reflectance spectra of CM2 chondrite Mighei irradiated with pulsed laser and implications for low-albedo asteroids and martian moons. 35th Lunar and Planetary Science Conference, p. 1279.

Moskovita, N.A., Abe, S., Pan, K.-S., Osip, D.J., Pefkou, D., Melita, M.D., Elias, M., Kitazato, K., Bus, S.J., DeMeo, F.E., Binzel, R.P., Abell, P.A., 2013. Rotational characterization of Hayabusa II target asteroid (162173) 1999 JU3. Icarus 224, Issue 1, 24 – 31, doi:10.1016/j.icarus.2013.02.009.

Muinonen, K., Parviainen, H., Naranen, J., Josset, J.L., Beauvivre, S., Pinet, P., Chevrel, S., Koschny, D., Grieger, B., Foing, B., and SMART-1 AMIE Team, 2011. Lunar mare single-scattering, porosity, and surface-roughness properties with SMART-1 AMIE. Astron. Astrophys. 531, A150, doi:10.1051/0004-6361/201016115Nakamura et al., 2020

Nakamura, T., Lantz, C., Nakauchi, Y., Amano, K., Brurnetto, R., Matsumoto, M., Kobayashi, S., Matsuoka, M., Noguchi, T., Matsumoto, T., Zolensky, M.E., 2020. Irradiation-energy Dependence on the Spectral Changes of Hydrous C-Type Asteroids Based on 4kev and 20kev He Exposure Experiments of Murchison CM Chondrite. Lunar and Planetary Sci. Conf. 51, 1310.

Nesvorny, D., Jedicke, R., Whiteley, R.J., Ivezic, Z., 2005. Evidence for asteroid space weathering from the Sloan Digital Sky Survey. Icarus 173, 132–152, doi: 10.1016/j.icarus.2004.07.026.

Okada, T., Fukuhara, T., Tanaka, S., Taguchi, M., Arai, T., Senshu, H., Sakatani, N., Shimaki, Y., Demura, H., Ogawa, Y., Suko, K., Sekiguchi, To., Kouyama, T., Takita, J., Matsunaga, T., Imamura, T., AWada, T., Hasegawa, S., Helbert, J., Müller, T.G. Hagermann, A., Biele, J., Grott, M., Hamm, M., Delbo, M., Hirata, N., Hirata, N., Yamamoto, Y., Sugita, S., Namiki, N., Kitazato, K., Arakawa, M., Tachibana, S., Ikeda, Hitoshi Ishiguro, M., Wada, K., Honda, C., Honda, R., Ishihara, Y.,Matsumoto, K., Matsuoka, M., Michikami, T., Miura, A., Morota, T., Noda, H., Noguchi, R., Ogawa, K., Shirai, K., Tatsumi, E., Yabuta, H., Yokota, Y., Yamada, M., Abe, M., Hayakawa, M., Iwata, T., Ozaki, M., Yano, H., Hosoda, S., Mori, O., Sawada, H., Shimada, T., Takeuchi, H., Tsukizaki, R., Fujii, A., Hirose, C., Kikuchi, S., Mimasu, Y., Ogawa, N., Ono, G., Takahashi, T., Takei, Yuto Yamaguchi, T., Yoshikawa, K., Terui, F., Saiki, T., Nakazawa, S., Yoshikawa, M., Watanabe, S., Tsuda, Y., 2020. Highly porous nature of a primitive asteroid revealed by thermal imaging. Nature 579, 518 - 522, doi:/10.1038/s41586-020-2102-6

Potin, S., Beck, P., Schmitt, B., Moynier, F., 2019. Some things special about NEAs: Geometric and environmental effects on the optical signatures of hydration. Icarus 333, 415 – 428, doi:10.1016/j.icarus.2019.06.026

Sakatani, N., Sugita, S., Honda, R., Morota, T., Yamada, M., Kameda, S., Tatsumi, E., Yokota, Y., Kouyama, T., Suzuki, H., Honda, C., Hayakawa, M., Yoshioka, K., Matsuoka, M., Cho, Y., Sawada, H., Ogawa, N., Miura, A., Okada, T., Tanaka, S., Senshu, H., Arai, T., Demura, H., Suko, K., Shimaki, Y., Sekiguchi, T., Takita, J., Fukuhara, T., Taguchi, M., Müller, T., Hagermann, A., Biele, J., Grott, M., Delbo, M., 2019. Surface Physical Condition of Asteroid Ryugu Using Close-up Optical and Thermal Images. Lunar and Planet. Sci. Conf. 50, 1732.

Sato, H., M.S. Robinson, B. Hapke, B.W. Denevi, A.K. Boyd, 2014. Resolved Hapke parameter maps of the Moon. J. Geophys. Res. Planets 119, Issue 8., 1775 – 1805.

Schröder, S.E., Mottola, S., Keller, H.U., Raymond, C.A., Russell, C.T., (2014) Reprint of: Resolved photometry of Vesta reveals physical properties of crater regolith. Planet. Space Sci. 103, 66-81.

Schröder, S.E., Li, J.-Y., Rayman, M.D., Joy, S.P., Polanskey, C.A., Carsenty, U., Castillo-Rogez, J.C., Ciarniello, M., Jaumann, R., Longobardo, A., McFadden, L.A., Mottloa, S.M., Sykes, M., Raymond, C. A., Russell, C.T., 2018. Cere's opposition effect observed by the Dawn framing camera. A&A, A201. doi:10.1051/0004-6361/201833596.

Shimaki, Y., Senshu, H., Sakatani, N., Okada,T., Fukuhara, T., Tanaka, S., Taguchi, M., Arai, T., Demura, H., Ogawa, Y., Suko, K., Sekiguchi, T., Kouyama, T., Hasegawa, S., Takita, J., Matsunaga, T., Imamura, T., Wada, T., Kitazato, K., Hirata, N., Hirata, N., Noguchi, R., Sugita, S., Kikuchi, S., Yamaguchi, T., Ogawa, N., Ono, G., Mimasu, Y., Yoshikawa, K., Takahashi, T., Takei, Y., Fujii, A., Takeuchi, H., Yamamoto, Y., Yamada, M., Shirai, K., Iijima, Y., Ogawa, K., Nakazawa, S., Terui, F., Saiki, T., Yoshikawa, M., Tsuda, Y., Watanabe, Y., 2020. Thermophysical Properties of the Surface of Asteroid 162173 Ryugu: Infrared Observations and Thermal Inertia Mapping. Icarus, 348, 113835. doi: 10.1016/j.icarus.2020.113835.

Shepard, M. K., Helfenstein, P., 2007. A test of the Hapke photometric model. Journal of Geophysical Research: Planets, 112(E3).

Shevchenko, V. G., & Belskaya, I. N. 2010. Opposition effect of dark asteroids: diversity and albedo dependence. EPSC 5, EPSC2010-738, European Planetary Science Congress 2010.

Shevchenko, V. G., Belskaya, I. N., Slyusarev., I. G., Krugly, Yu. N, Chiorny, V. G., Gaftonyuk, N. M., Donchev, Z., Ivanova, V., Ibrahimov, M. A., Ehgamberdiev, Sh. A., Molotov, I. E., 2012. Opposition effect of Trojan asteroids. Icarus, 217, 202-208. doi:10.1016/j.icarus.2011.11.001

Shkuratov, Y. G., Helfenstein, P., 2001. The opposition effect and the quasi-fractal structure of regolith: I. Theory. Icarus, 152, 96 – 116, doi:10.1006/icar.2001.6630.

Shkuratov, Y. G., Starukhina, L. V., Kreslavsky, M. A., Opanasenko, N.V., Stankevich, D.G., Shevchenko, V.G., 1994. Principle of undulatory invariance in photometry of atmospherelisss celelstial bodies. Icarus, 109,168 – 190, doi:10.1006/icar.1994.1084.

Shkuratov, Y. G., Kreslavsky, M. A., Ovcharenko, A. A., Stankevich, D.G., Zubko, E.S., Pieters, C., Arnold, G., 1999. Opposition effect from Clementine data and mechanisms of backscatter. Icarus, 141, 132 – 155, doi:10.1006/icra.199.6154.

Shkuratov, Y., Kaydash, V., Korokhin, V., Velikodsky, Y., Petrov, D., Zubko, E., Stankevich, D., Videen, G., 2012. A critical assessment of the Hapke photometric model. J. Quant. Spectr. Rad.Transf., 113, 2431 – 2456, doi:10.1016/j.qsrt.2012.04.010.

Souchon, A.L., Pinet, P.C., Chevrel, S.D., Daydou, Y.H., Baratoux, D., Kurita, K., Shepard, M.K., Helfenstein, P. 2011. An experimental study of Hapke's modeling of natural granular surface samples. *Icarus* **215**, 313 – 331.

Spjuth, S., Jorda, L., Lamy, P.L., Keller, H.U., Li, J.-Y., 2012. Disk-resolved photometry of Asteroid (2867) Steins. Icarus 221, 1101 – 1118.

Tatsumi, E., Kouyama, T., Suzuki, H., Yamada, M., Sakatani, N., Kameda, S., Yokota, Y., Honda, R., Morota, T., Moroi, K., Tanabe, N., Kamiyshihara, H., Ishida, M., Yoshioka, K., Sato, H., Honda, C., Hayakawa, M., Kitazato,K., Sawasa, H., Sugita, S., 2019. Updated inflight calibration of Hayabusa2's optical nafivation camera (ONC) for scientific observations during the cruise phase. Icarus, 325, 153- 195.

Tatsumi, E., Domingue, D., Hirata, N., Kitazato, K., Vilas, F., Lederer, S., Weissman, P.R., Lowry, S.C., Sugita, S., 2018. Vis-NIR disk-integrated photometry of asteroid 25143 Itokawa around opposition by AMICA.Hayabusa. Icarus 311, 175-196.

Tatsumi, E., Domingue, D., Yokota, Y., Schröder, S., Kuroda, D., Ishiguro, M., Hasegawa, S., Hiroi, T., Honda, R., Hemmi, R., Le Corre, L., Sakatani, N., Morota, T., Yamada, M., Kameda, S., Koyama, T., Suzuki, H., Cho, Y., Yoshioka, K., Matsuoka, M., Honda, C., Hayakawa, M., Hirata, N., Hirata, N., Yamamoto, T., Vilas, F., Takato, N., Yoshikawa, M., Abe, M., Sugita, S., 2020. Global photometric properties of (162173) Ryugu. Accepted, A&A, doi: 10.1051/0004-6361/201937096

Thompson, M. S., Loeffler, M. J., Morris, R. V., Keller, L. P., & Christoffersen, R. 2019. Spectral and chemical effects of simulated space weathering of the Murchison CM2 carbonaceous chondrite. Icarus, 319, 499 – 511, doi:10.1016/j.icarus.2018.09.022

Thompson, M. S., Morris, R.V., Clemett, S.J., Loeffler, M.J., Trang, D., Keller, L.P., Christoffersen, R., Agresti, D.G., 2020. The effect of progressive space weathering on the organic and inorganic components of a carbonaceous chondrite. Icarus 346, 113775, doi:10.1016/j.icarus.2020.113775.

Tsuda, Y., Saiki, T., Terui, F., Nakazawa, S., Yoshikawa, M., Watanabe, S., Hayabusa2 Project Team, 2020. Hayaubsa2 mission status: Landing, roving and cratering on asteroid Ryugu. Acta Astronautica, 171, 42-54. doi: 10.1016/j.actaastro.2020.02.035

Vernazza, P., Fulvio, D., Brunetto, R., Emery, J.P., Dukes, C.A., Cipriani, F., Witasse, O., Schaible, M.J., Zanda, B., Strazzulla, G., Baragiola, R.A., 2013. Paucity of Tagish Lake-like parent bodies in the asteroid belt and among Jupiter Trojans. Icarus 225, 517–525. doi:10.1016/j.icarus.2013.04.019

Yokota et al. 2020 Opposition observations of 162173 Ryugu: Normal albedo map highlights variations in regolith characteristics. In preparation (to be submitted concurrently with this manuscript to the same journal).